

**ANALYZING SHAPE AND RESIDUAL POSE OF
SUBCORTICAL STRUCTURES IN BRAINS OF
SUBJECTS WITH SCHIZOPHRENIA**

by
Shreyas Padhy

**A thesis submitted to The Johns Hopkins University
in conformity with the requirements for the degree of
Master of Science in Engineering**

Baltimore, Maryland

May, 2019

© 2019 Shreyas Padhy

All rights reserved

Abstract

This study focuses on four anatomical features of subcortical structures associated with schizophrenia: volume, surface area, shape and residual pose. Being a chronic mental disorder, schizophrenia affects 1% of the local population and is one of the leading causes of disability around the world. However, the symptoms of schizophrenia appear and spread gradually, and robust mathematical and statistical models of disease progression have the capability to help find meaningful biomarkers of schizophrenia, which may aid researchers and clinicians to develop potentially novel treatments of the disease.

This study used the open-source Schizconnect dataset, and data was automatically segmented by the MRICloud pipeline, following which scans were mapped to a common surface template using unbiased diffeomorphic mapping. The first part of this study focuses on global volumetric and local surface analysis of 6 subcortical structures; the Amygdala, the Hippocampus, the Caudate, the Putamen, the Globus Pallidum, and the Thalamus. Significant total volume and regional surface area changes are seen in the hippocampus and thalamus, and reduced atrophy is seen in the diseased subjects compared to the control subjects for the hippocampus, globus pallidum, and thalamus, whereas increased atrophy is seen for the diseased subjects compared to the control subjects in the amygdala, caudate and putamen.

This study also develops a mathematical formulation for residual pose analysis, describing a robust algorithm to obtain residual pose parameters from MR scans using general orthogonalized Procrustes analysis, and modelling of rigid transformation matrices as Lie Groups. Cross-sectional and longitudinal analysis is performed on these residual pose

parameters, and significant differences are seen in the amygdala, hippocampus, caudate and globus pallidum for the cross-sectional study, whereas significant changes are seen in the amygdala, hippocampus, and caudate for the longitudinal study.

This study aims to be the first known exploration of residual pose to characterize longitudinal development of schizophrenia and analyze complementary features to traditional shape analysis that have previously been discarded in the exploration of this disease, while also developing a robust mathematical formulation for pose analysis, in order to contribute to further research that has the potential to find biomarkers of disease onset and progression from non-invasive imaging modalities such as MRI.

Primary Reviewer : J. Tilak Ratnanather, PhD

Secondary Reviewer : Patrick Barta, MD, PhD

Secondary Reviewer : Siamak Ardekani, PhD

Acknowledgments

I would like to thank my co-advisors Dr. Michael Miller and Dr. Tilak Ratnanather for being excellent mentors that have introduced me to cutting-edge research at the intersection of neuroscience and biomedical engineering, while also being supportive and providing me every opportunity to grow as a student and researcher.

I am also grateful to the many excellent peers and mentors I have met at the Center for Imaging Science, who have guided me throughout my research in my time at Johns Hopkins University. Dr. Daniel Tward was instrumental in helping me with my research ideas for this thesis, and I am very thankful for my discussions with fellow lab members Hubert Liu and Sue Kulason, as well as Dr. Kwame Kutten.

I am always indebted to my family and friends, who have been pillars of support throughout my graduate education, and every milestone of mine is shared with them.

Shreyas Padhy

May 9, 2019

Table of Contents

Table of Contents	v
List of Tables	vii
List of Figures	viii
1 Introduction	1
2 Methods and Design	5
2.1 Scientific Notation	5
2.2 Subcortical Segmentation	5
2.3 Surface Triangulation	6
2.4 Surface Template Estimation	7
2.5 Diffeomorphic Mapping of Images	10
2.5.1 Diffeomorphisms and Vector Spaces	10
2.5.2 Unbiased longitudinal mapping	11
2.6 Shape Analysis	13
2.6.1 Residual Pose Analysis	13
2.6.1.1 Procrustes Mean Shape Calculation	14
2.6.1.2 Relative Pose Calculation	15

2.6.1.3	Mean Pose Calculation	17
2.6.1.4	Residual Pose Calculation	18
2.6.2	Volume and Local Surface Analysis	19
2.7	Statistical Modelling	20
2.7.1	Cross-sectional Modelling	20
2.7.1.1	ANCOVA Analysis	20
2.7.1.2	MANCOVA Analysis	22
2.7.2	Longitudinal Modelling	22
2.7.3	Controlling for familywise error rate	23
2.7.3.1	Bonferroni Correction	24
2.7.3.2	Permutation Testing	24
3	Volumetric and Local Surface Analysis	27
3.1	Volume Regressions over Time	27
3.2	Volumetric and Local Surface Analysis	37
3.2.1	Longitudinal modelling with mixed-effects models	37
4	Residual Pose Analysis	46
4.1	Residual Pose analysis	46
4.1.1	Cross-sectional Analysis	47
4.1.2	Longitudinal Analysis	50
5	Discussion and Conclusion	57
5.1	Limitations	61
5.2	Future Work	62

List of Tables

2.1	Notation	5
2.2	Demographic information for the Schizconnect dataset	6
3.1	Significance values for mixed-effects modelling of log(volume) and log(surface Jacobians) and percentage ratios of significant vertices, for both unique STEs for left and right hemispheres (left), and combined STEs (right). <i>p</i> -values below 0.05 are reported in bold	39
3.2	Atrophy Rates for the Control and Disease groups in % per year for subcortical structures for both unique STEs for the left and right hemispheres (left), and combined STEs (right)	42
4.1	Significance values for cross-sectional analysis for residual pose parameters p_i . Statistically significant pose parameters are reported in bold.	48
4.2	Significance values for longitudinal mixed-effects modelling of residual pose parameters for the unique STE paradigm for left and right hemisphere	50
4.3	Significance values for longitudinal mixed-effects modelling of residual pose parameters for the combined STE paradigm	51

List of Figures

2.1	Preprocessing pipeline comprising of (I) Subcortical Segmentation of a structural MR Image using MRICloud, followed by (II) Surface Triangulation of binary segmentations of subcortical structures	7
2.2	Preprocessing steps (III) for Surface Template Estimation with the unique paradigm (left) and the combined paradigm (right)	9
2.3	Proposed unbiased longitudinal matching method, where the geodesic trajectory determined by p^0 maps the surface template onto the patient-specific template in the patient's time-series at $t = t_0$, and the geodesic determined by p^1 maps the patient-specific template to individual scans for the patient. Figure reproduced with permission from the authors ((Tward, Miller, and Initiative, 2017)	12
2.4	Following the procedure described in Figure 2.1 and Figure 2.2 and the unbiased longitudinal mapping step, we obtain surfaces that are the surface template non-linearly deformed to match each surface in the population, with one-to-one correspondence. Iterative procedure for Procrustes Mean Shape calculation is then defined by the above procedure.	14
2.5	Procedures to calculate the relative poses (left), and the mean pose through an iterative procedure (right) upon obtaining the Procrustes mean shape for the population	17

3.1	Line-plots of binary segmentation volumes for control subjects with 2 scans (top-left) and 3 scans (bottom-left), and diseased subjects with 2 scans (top-right) and 3 scans (bottom-right), for the Amygdala, Hippocampus, and Caudate.	29
3.2	Line-plots of binary segmentation volumes for control subjects with 2 scans (top-left) and 3 scans (bottom-left), and diseased subjects with 2 scans (top-right) and 3 scans (bottom-right), for the Putamen, Globus Pallidum, and Thalamus.	30
3.3	Line-plots of triangulated surface volumes for control subjects with 2 scans (top-left) and 3 scans (bottom-left), and diseased subjects with 2 scans (top-right) and 3 scans (bottom-right), for the Amygdala, Hippocampus, and Caudate.	31
3.4	Line-plots of triangulated surface volumes for control subjects with 2 scans (top-left) and 3 scans (bottom-left), and diseased subjects with 2 scans (top-right) and 3 scans (bottom-right), for the Putamen, Globus Pallidum, and Thalamus	32
3.5	Histograms and best-fit probability distribution curves for volume slopes, for the Amygdala, Hippocampus, and Caudate. Green refers to the control group and red refers to the diseased group	34
3.6	Histograms and best-fit probability distribution curves for volume slopes, for the Putamen, Globus Pallidum, and Thalamus. Green refers to the control group and red refers to the diseased group	35
3.7	Surface p -value plots showing statistically significant vertices for the left surface template (left), the right surface template (center), and the combined surface template (right); for the Amygdala, Hippocampus, and Caudate . .	44

3.8	Surface p -value plots showing statistically significant vertices for the left surface template (left), the right surface template (center), and the combined surface template (right); for the Putamen, Globus Pallidum, and Thalamus	45
4.1	Superimposed plots of the calculated Procrustes mean shape for the control group (green) and the diseased group (red); for the Amygdala, Hippocampus, and Caudate	53
4.2	Superimposed plots of the calculated Procrustes mean shape for the control group (green) and the diseased group (red); for the Putamen, Globus Pallidum, and Thalamus	54
4.3	Superimposed plots of the calculated Procrustes mean shape for the control group (green) and the diseased group (red) along the axial section	55
4.4	Superimposed plots of the calculated Procrustes mean shape for the control group (green) and the diseased group (red) along the coronal section	56

Chapter 1

Introduction

Schizophrenia is a chronic mental health disorder that affects a person's emotions, memories and behaviours, resulting in manifestations of false beliefs, delusions, hallucinations (both auditory and visual), and impaired thinking. Despite being a severe disorder that affects around 1% of the general population (Kessler et al., 2005) and being one of the top 15 causes of disability in individuals worldwide (Vos et al., 2017), the neuropathology of schizophrenia remains unknown, and the conclusions from multiple neuropathological studies have been conflicting (Shenton et al., 2001). Over the years, with the increasing improvements being made in medical image acquisition and analysis, non-invasive techniques such as CT and MRI have been used to detect possible biomarkers of neuropathological change in schizophrenia. There have been studies showing that schizophrenia may be triggered by and affected by both environmental and genetic factors, and there is significant familial risk in the onset of schizophrenia for first-degree relatives and second-degree relatives (Patel et al., 2014). There is considerable risk of the development of schizophrenia in a person with both parents showing symptoms of the disease, however at the same time, there have been studies showing the dependence of the onset on the disease on prenatal developmental conditions, history of drug abuse, and even residential environments (Siever and Davis, 2004, Womer et al., 2014).

Several techniques involving the analysis of subcortical brain anatomy have previously been used in the analysis of schizophrenia, focusing on both raw volumetric and local morphometric changes in different regions of the brain. Structural MRI measurements have specifically been shown to be able to detect statistically significant differences between schizophrenic patients and controls for cortical, subcortical, and regional volumes and thickness in the brain (Van Rheenen et al., 2017). There have been studies showing that certain subcortical structures such as the amygdala, thalamus, and hippocampus decrease in volume in schizophrenia (Prestia et al., 2011), whereas the globus pallidum and putamen increase in volume (Ellison-Wright and Bullmore, 2010). There have been studies with differing results on the effect of the disease on the volume and morphometry of the caudate, with studies showing both an increase in volume for the diseased population (Ellison-Wright and Bullmore, 2010; Mamah et al., 2007), and a decrease in volume (Watson et al., 2012; Ebdrup et al., 2010). Despite being a chronic mental disorder, schizophrenia has a gradual progression from onset in early adulthood to chronic symptoms developing later. In order to model this longitudinal progression of the disease, there has been significant research in discovering potential biomarkers of longitudinal change from structural data measured through non-invasive imaging techniques such as MRI (Heilbronner et al., 2016; Szöke et al., 2008).

More recently, in the study of Alzheimer's Disease, there are studies which show that volume and local morphological changes may not capture certain information about the progression of disease that may serve as potential biomarkers (Bossa, Zacur, and Olmos, 2011). Previously, there have been a variety of shape features that have been used in the broad study of both Alzheimer's Disease and schizophrenia, including landmark coordinates (Csernansky et al., 2004), radial atrophy maps (Querbes et al., 2009; Thompson et al., 2007), and medial representations (Styner et al., 2004). In all of these studies, shape features are extracted by first discarding any pose information by aligning scans to

common atlases. In fact, it is common in shape analysis theory to attribute all geometrical information about an object invariant to its pose to the shape information. However, there has been recent work suggesting that pose information of anatomical structures may serve as complementary features to shape and volume (Rao, Aljabar, and Rueckert, 2008).

Rao et al.'s studies suggest that information about the relative pose of different subcortical structures within a population of subjects contains useful information that may contribute to the diagnosis, prognosis and monitoring of neurodegenerative diseases such as Alzheimer's, and possibly by extension, schizophrenia. The earliest work in pose analysis was performed by creating point distribution models for subcortical nuclei, which were treated as joint shape and pose descriptors (Rao, Aljabar, and Rueckert, 2008). The first work in introducing a formal statistical model for pose descriptions was introduced to model subcortical structures for healthy subjects (Bossa and Olmos, 2006), which was then extended for the study of Alzheimer's Disease (Bossa and Olmos, 2007). These statistical models have also been extended to perform longitudinal studies of autism (Styner et al., 2006; Gorczowski et al., 2010), and analysis of the pose of the thalamus in preterm neonates (Lao et al., 2013).

In this study, we perform a comprehensive and complementary analysis of volume, surface area, relative shape and residual pose information for the purposes of understanding the progression and morphology of schizophrenia, using the open-source Schizconnect dataset. By analyzing both shape information and relative pose simultaneously, we explore the correlation between features returned by both methods of analysis. Further, in order to model the longitudinal progression of schizophrenia and its effects on morphology and pose in subcortical structures of the human brain, we use an unbiased longitudinal diffeomorphic mapping algorithm, along with generalized mixed-effects models to study whether there are any statistically significant differences across the healthy and

diseased groups in the Schizconnect dataset. We first describe the dataset, followed by the preprocessing pipeline used to process the dataset. We then formalize and develop an algorithm to perform residual pose analysis with 3D binary segmentations of subcortical structures, followed by some statistical methods to analyse both residual pose and other morphological features. For shape and volumetric analysis, we also explore the advantages and drawbacks to using surface templates that are either unique to the left and right hemispheres, or combined across the two hemispheres of the human brain, and report results for the same. To our knowledge, relative pose information has not been used to study the effects of schizophrenia on the human brain, and we hope to find meaningful sensitive and specific markers of early schizophrenic disease progression, which may motivate and aid researchers and clinicians to develop potentially novel treatments of the disease, while being able to non-invasively monitor the effectiveness of these treatments on brain morphology.

Chapter 2

Methods and Design

2.1 Scientific Notation

Throughout the following chapters, the following scientific notation has been used, which is summarized in Table 2.1 for easy reference.

a	A scalar (integer or real)
\mathbf{a}	A vector
A	A matrix
I	A binary image
$S = (V, F)$	A triangulated surface
T	A transformation matrix
φ	A diffeomorphism
u, v	Vector fields

Table 2.1: Notation

2.2 Subcortical Segmentation

For the purposes of this study, we used MRICloud to process and segment the structural MRI data from the Schizconnect Dataset. MRICloud is a high-throughput web-based cloud service that performs automated segmentation of brain MRI, and subsequent quantification analysis (Mori et al., 2016). Patient data was obtained from the Schizconnect website in the form of NifTi files (*Schizconnect Website*; Wang et al., 2015; Wang et al., 2016). These images were uploaded to the MRICloud website, where they were automatically segmented into

286 discrete parcellations of the human brain based on the Multiple Atlas Likelihood Fusion (MALF) algorithm (Tang et al., 2013; Mori et al., 2016). The MALF algorithm works by aggregating label information from multiple human atlases to generate the final segmentation. Multiple atlases are deformed to the target image simultaneously, and for each atlas, a voxel in the target image is attributed the label with the highest probability based on the likelihood-fusion algorithm. Finally, based on voxel attributions from each individual atlas, a global voting is performed to pick the label that is predicted by the most atlases. Studies have shown that the MALF algorithm works better in practise, compared to other standard approaches such as STAPLE (Warfield, Zou, and Wells, 2004) and spatial STAPLE (Asman and Landman, 2012). There has also been work to show that MRICloud achieves better overall performance in segmenting subcortical structures such as the hippocampus and amygdala using the MALF algorithm compared to other web-based segmentation pipelines such as Freesurfer and FSL (Tang et al., 2013). Following automated binary segmentation by the MRICloud pipeline, we performed manual quality control by observing the binary segmentations and excluding subjects where any of their scans were noisy, or had artefacts regarding the segmentation step, resulting in discontinuous volumes or volumes where the surfaces had high variance. A total of 21 subjects were excluded after manual quality control, and the demographic information for the remaining subjects is presented in Table 2.2

	Control	Strict Schizophrenia
Number of subjects	66	48
Number of scans	157	110

Table 2.2: Demographic information for the Schizconnect dataset

2.3 Surface Triangulation

After obtaining binary segmentations for the subcortical structures, we then perform restricted Delauney triangulation (Shewchuk, Dey, and Cheng, 2016) to obtain triangular

surface meshes that roughly correspond to the 3D subcortical shape and surface represented by the binary segmentation. Given a binary voxel segmentation image of a surface $I \in \{0,1\}^{K \times L \times M}$, where K , L , and M are the dimensions in voxels of the 3D MRI scan, using restricted Delauney triangulation, we obtain a triangulated surface $\mathcal{S} = (\mathbf{V}, \mathbf{F})$ with N_v vertices and N_f faces. Here, $\mathbf{V} \in \mathbb{R}^{N_v \times 3}$ are the 3-dimensional vertices of the surface, and $\mathbf{F} \in \mathbb{Z}^{+N_f \times 3}$ are the triangular faces, ordered as 3-tuples of vertex numbers with 3-dimensional coordinates given in \mathbf{V} . The preprocessing pipeline, comprised of the subcortical segmentation and surface triangulation steps are visualized in Figure 2.1.

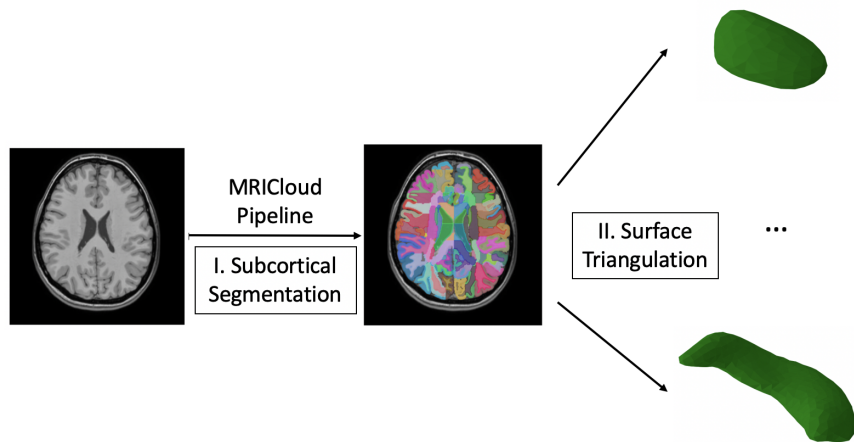


Figure 2.1: Preprocessing pipeline comprising of (I) Subcortical Segmentation of a structural MR Image using MRICloud, followed by (II) Surface Triangulation of binary segmentations of subcortical structures

2.4 Surface Template Estimation

Performing restricted Delauney triangulation gives us representations of the subcortical structures as 3D triangulated mesh surfaces ($\mathcal{S}^{(i)} = (\mathbf{V}^{(i)}, \mathbf{F}^{(i)})$ for $i = 1, \dots, N$). Before we can perform diffeomorphic image mapping, we need to calculate a surface template for each subcortical structure, to serve as a base for the diffeomorphic image mapping algorithm. To estimate a surface template, a statistical model is constructed that models the generation and observation of random triangular surfaces using a geodesic shooting approach, following which a mode approximation EM algorithm is used to determine the

template surface (Ma, Miller, and Younes, 2010).

The MRICloud service provides a surface template estimation tool that uses the above-mentioned algorithm to automatically calculate a surface template based on a subset of 96 triangulated surfaces from the population, and a hypertemplate surface. We specifically select 96 surfaces as that is the maximum number of surfaces that MRICloud simultaneously calculates surface templates from, based on the memory capacity of the MRICloud resource. The subset and hypertemplate selection are performed as follows

1. For each subject at their baseline scan, the total volume of all the subcortical structures is calculated, and the subjects are ordered on the basis of their volumes.
2. The subject with the median total subcortical volume is selected as the hypertemplate subject.
3. The triangulated surface for this hypertemplate subject is selected as the hypertemplate.
4. The 48 surfaces below and above the hypertemplate in the ordering are selected as the subset of 96 surfaces used for Surface Template Estimation.

Based on the preliminary volume regression analysis performed in section 3.1, it was seen that there was significant variation in the volume trends across subjects, across the left and right hemispheres. In order to smooth out variation due to the quality of both the binary segmentations and the triangulations, and to explore the dependence on downstream analysis on the surface template estimation step, two methods of surface template estimation were used, which are described below, and also graphically represented in Figure 2.2:

1. **Unique surface templates for each hemisphere:** In this paradigm of surface template estimation, the hypertemplate and the 96 structures chosen as a subset of the population were kept restricted to either the left or right hemispheres alone. For

example, 96 surfaces of the left thalamus were chosen along with a left thalamus hypertemplate to calculate a surface template for the left thalamus specifically. Therefore, for each subcortical structure, there was an independent surface template for the left structure and the right structure respectively. For 14 subcortical structures, this results in 28 surface templates. Subsequent diffeomorphic mapping is then performed from the left surface template to the left surfaces, and so on.

- 2. Combined surface template for each subcortical structure:** In this paradigm of surface template estimation, a common surface template was estimated for each subcortical structure, by combining both the left and right surfaces. For example, 48 surfaces for the left thalamus and 48 surfaces for the right thalamus were chosen along with a thalamus hypertemplate, to calculate a surface template for the thalamus. For 14 subcortical structures, this results in 14 surface templates. Subsequent diffeomorphic mapping is then performed from the surface template to both the left surfaces and right surfaces. The advantage of combined STE is that for each subcortical structure, we obtain a one-to-one mapping across the structures in the left and right hemispheres, allowing us to perform analysis that is independent of the hemisphere, and in the process smooth out some variation that may be introduced by treating the left and right structures as independent entities.

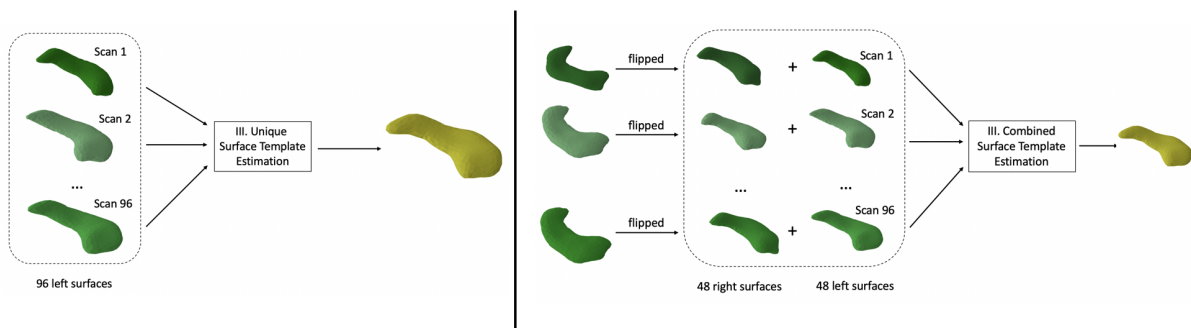


Figure 2.2: Preprocessing steps (III) for Surface Template Estimation with the unique paradigm (left) and the combined paradigm (right)

2.5 Diffeomorphic Mapping of Images

After obtaining a surface template for each subcortical structure, a longitudinal diffeomorphic algorithm is used to perform an unbiased mapping of each binary segmentation to the surface template, in order to obtain a one-to-one correspondence between structures across the population. It has been shown previously that traditional longitudinal mapping techniques that map a template onto baseline images and then follow-up images tend to overestimate atrophy rates in subcortical structures such as the entorhinal cortex (Tward et al., 2017a). In order to remove this source of bias, an algorithm is used where a patient-specific template is inserted into a time series at a specific point that is estimated from data, following which a time-varying mapping is calculated connecting each image in the time series (Tward, Miller, and Initiative, 2017). The details of the algorithm are described below.

2.5.1 Diffeomorphisms and Vector Spaces

In the field of computational anatomy (Grenander and Miller, 1998), the population of anatomical shapes can be defined as the action of diffeomorphisms on a particular shape (or template), where these diffeomorphisms are generated by a time dependent flow of smooth vector fields.

We can formalize this by defining diffeomorphisms $\varphi : \Omega \subset \mathbb{R}^3 \rightarrow \Omega$, which are generated from flows of smooth vector fields $v : \Omega \rightarrow \mathbb{R}^3$, such that

$$\dot{\varphi} = v(\varphi), \varphi_0 = \text{Identity} \quad (2.1)$$

To ensure that the vector fields are sufficiently smooth, they are considered to be embedded in a Hilbert space of smooth functions V , where the inner product in this space is defined

as

$$\langle u, v \rangle = \langle Lu, Lv \rangle_{L^2} \quad (2.2)$$

$$= \int_{\Omega} (L^*Lu)^T(x)v(x)dx \quad (2.3)$$

where L is a differential operator with its' corresponding adjoint L^* . The form of L is specified by setting the kernel (or inverse) of the operator L^*L as

$$K(x, x') = \exp\left(-\frac{1}{2\sigma_V^2}|x - x'|^2\right) \quad (2.4)$$

where $\sigma_V = 6\text{mm}$. Further, we define a quantity $p = L^*Lv$ called the *momentum*, which results in the vector fields being represented as $v = K.p$. Finally, the norm in this space is defined as

$$\|v\|_V^2 = \langle v, v \rangle_V \quad (2.5)$$

$$\text{Equivalently, } \|p\|_{V^*}^2 = \|K.p\|_V^2 \quad (2.6)$$

In this space of diffeomorphisms, shortest path trajectories (or geodesics) are expressed in the form of the following equation

$$\dot{p} = -Dv^T(\varphi)p \quad (2.7)$$

2.5.2 Unbiased longitudinal mapping

For unbiased longitudinal mapping, we consider two geodesic trajectories, one that maps the template onto the time series (determined by p^0 , and one that passes through the time series (determined by p^1). The corresponding diffeomorphisms are given by

$$\varphi_s^0, s \in [0, 1], \quad \varphi_t^1, t \in \text{elapsed time in years} \quad (2.8)$$

The goal is to map the surface template I_0^0 onto the time-series of binary segmentations J^i that represent subcortical structures, sampled at times t_i (elapsed time in years), for $i \in \{1, \dots, T\}$. The corresponding cost function to solve for this system of flows is given by

$$E = \sum_{i=1}^T \left[\frac{1}{2T\sigma_{p^0}^2} \left\| p_0^0 \right\|_{V^*}^2 + \frac{1}{2\sigma_{p^1}^2} \left\| p_0^1(t_i - t_0) \right\|_{V^*}^2 + \frac{1}{2\sigma_I^2} \left\| I_{t_i}^1 - J^i \right\|_{L_2}^2 \right] \quad (2.9)$$

where $I_{t_i}^1 = \exp(v_0^1(t_i - t_0)) \cdot \exp(v_0^0) \cdot I_0^0$. Upon solving this optimization problem, we obtain diffeomorphic flows that map the surface template onto each binary segmentation. The unbiased longitudinal mapping algorithm is also represented in Figure 2.3 in terms of the two geodesics being calculated.

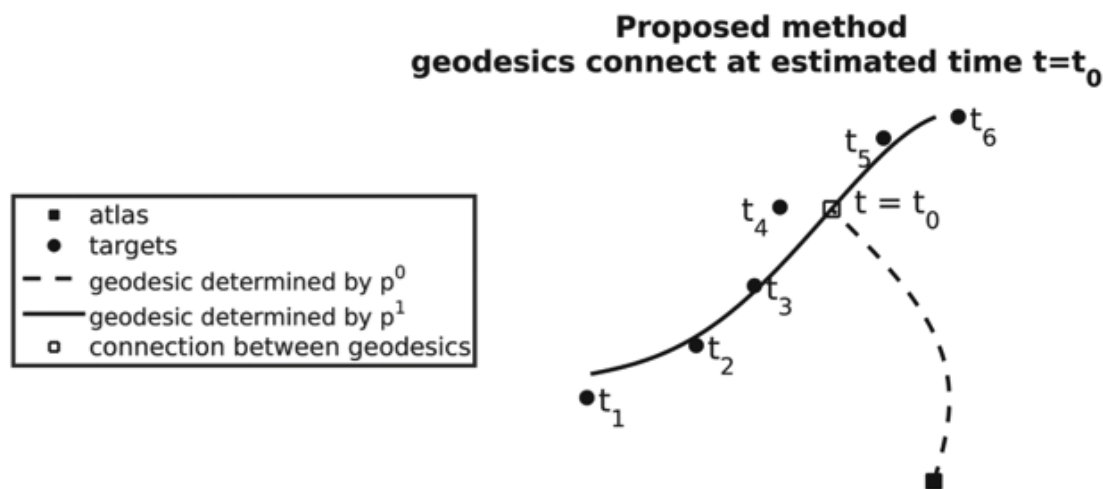


Figure 2.3: Proposed unbiased longitudinal matching method, where the geodesic trajectory determined by p^0 maps the surface template onto the patient-specific template in the patient's time-series at $t = t_0$, and the geodesic determined by p^1 maps the patient-specific template to individual scans for the patient. Figure reproduced with permission from the authors ((Tward, Miller, and Initiative, 2017))

2.6 Shape Analysis

After performing diffeomorphic image mapping of each surface template to each subcortical structure in the population, we obtain subcortical structures $V^{(i)} \in \mathbb{R}^{N_V \times 3}$ for $i = 1, \dots, N$ with one-to-one correspondence between vertices, that are rigidly aligned to the surface template. We are now equipped to perform a joint analysis of a set of triangulated meshes that carry shape information about the subcortical structures under study. In this study, we focus on three forms of structural analysis: (1) a residual pose analysis, (2) volumetric analysis, and (3) local atrophy analysis. These methods are described in further detail below:

2.6.1 Residual Pose Analysis

According to theories in shape analysis, the shape of any object is often defined as the geometric information contained by that object that are invariant to pose, where pose is defined as information about the location, orientation and size of the object (Bossa, Zacur, and Olmos, 2011). According to this definition, the entirety of information that is contained by an object can be characterized by both the pose and shape information, which are often complementary. The pose itself can be decomposed into a global pose and a residual pose. Global pose in the context of subcortical shapes measured through MR images often accounts for the position and orientation of patients within the scanner and other confounding factors which don't contain meaningful information. However, after accounting for global pose, the remaining residual pose information has been shown to hold useful information for diagnosis, prognosis and monitoring (Rao, Aljabar, and Rueckert, 2008; Bossa and Olmos, 2006; Bossa and Olmos, 2007).

In this study, we account for global pose confounding factors by aligning MR images to a reference atlas using 12 degrees of freedom. The residual pose for each subcortical

structure is calculated using generalized orthogonal Procrustes analysis, which is a rigid shape analysis technique that uses isomorphic scaling, translation, and rotation to find the "best" fit between multiple shapes (Ross, 2004). Firstly, a reference Procrustes mean shape is calculated for the population using an iterative procedure described in subsection 2.6.1.1. After obtaining the Procrustes mean, the relative pose of each shape is calculated with respect to the Procrustes mean, following which a mean pose is calculated from the relative poses. Finally, the residual pose of each shape is calculated by subtracting the mean pose from each relative pose. The details of each individual step are described in further detail in the subsequent subsections.

2.6.1.1 Procrustes Mean Shape Calculation

The Procrustes mean for a collection of N surfaces with one-to-one point correspondence is performed in an iterative procedure, which is described in Algorithm 1. A graphical representation of the algorithm is also depicted in Figure 2.4.

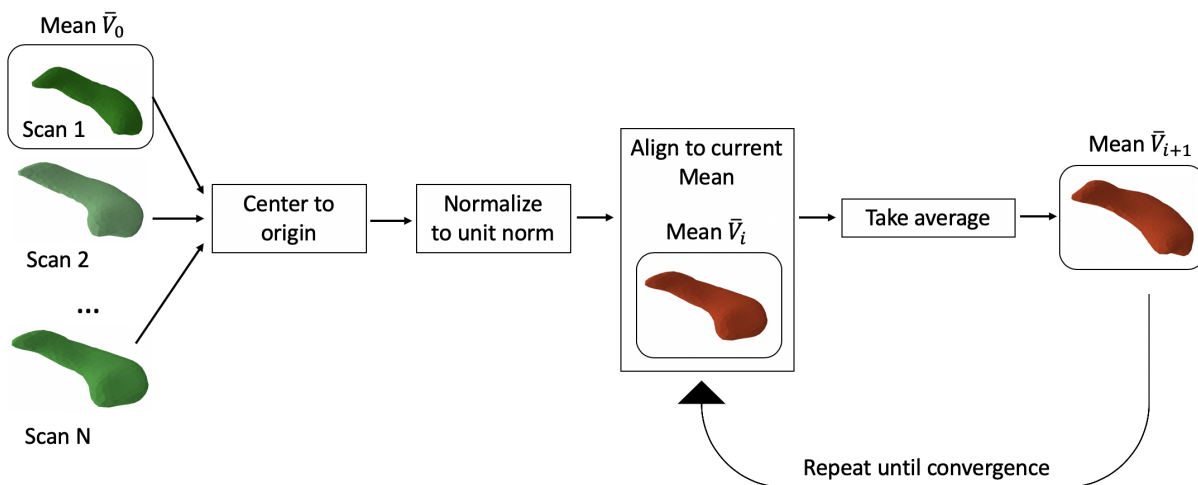


Figure 2.4: Following the procedure described in Figure 2.1 and Figure 2.2 and the unbiased longitudinal mapping step, we obtain surfaces that are the surface template non-linearly deformed to match each surface in the population, with one-to-one correspondence. Iterative procedure for Procrustes Mean Shape calculation is then defined by the above procedure.

2.6.1.2 Relative Pose Calculation

On obtaining the Procrustes mean shape, we can finally begin performing shape analysis using the residual poses of shapes across a population. We motivate the subsequent residual pose analysis by formulating a theory of geometric transformations for pose.

Two geometric objects (or structures) A and B are considered to have the same shape if there exists a geometric transformation \mathbf{T} that maps A onto B , which is equivalent to $\mathbf{T}(A) = B$. For the purposes of anatomical shapes, we consider similarity transformations that account for translation, rotation, and scaling effects, as these transformations have the desirable property of belonging to Lie groups (Bossa, Zacur, and Olmos, 2011). The advantage of working with Lie groups is that they are Riemannian manifolds, and therefore this gives us the ability to represent transformation matrices in terms of a vector space, where the addition and scalar multiplication properties are well defined, which allows us to calculate a mean transformation matrix (or mean pose). For the Lie Group \mathbb{G} , the tangent space that exists at a point e given by $\mathfrak{g} = T_e\mathbb{G}$ is a vector space. Assuming a vector field $v \in \mathfrak{g}$, we are specifically interested in a smooth and invertible mapping (or diffeomorphism) that maps from \mathfrak{g} to \mathbb{G} and its corresponding inverse, in order to map the transformation matrices into a vector space. For matrix groups, a natural choice is the exponential map ($\exp : \mathfrak{g} \rightarrow \mathbb{G}$), and its inverse, the logarithmic map ($\log : \mathbb{G} \rightarrow \mathfrak{g}$), as this mapping, known as the Log-Euclidean framework, contains certain desirable properties that make performing computations with elements from a Lie group much easier (Arsigny et al., 2006).

Considering the population of surfaces $\mathcal{S}^{(i)} = (\mathbf{V}^{(i)}, \mathbf{F}^{(i)})$ obtained through the preprocessing pipeline, a similarity transformation can operate on a surface by simply operating on the matrix of vertices, while keeping the matrix of faces untouched, as that refers

to the relative ordering of vertices that make up faces, which is invariant to similarity transformations. Therefore, a similarity transformation is characterized as

$$\mathbf{T}(V) = s\mathbf{R}V + \mathbf{b} \quad (2.15)$$

where $s \in \mathbb{R}^+$ is a uniform scaling across all three dimensions, $\mathbf{b} = (b_x, b_y, b_z)^T \in \mathbb{R}^3$ is the translation vector in three dimensions, and $\mathbf{R} \in SO(3)$ is the orthogonal rotation matrix in three dimensions, for a total of seven degrees of freedom. The transformation can also be represented in homogeneous coordinates as the following matrix

$$\mathbf{T}(s, \mathbf{R}, \mathbf{b}) = \begin{pmatrix} s\mathbf{R} & \mathbf{b} \\ \mathbf{0}^T & 1 \end{pmatrix} \in \mathbb{R}^{4 \times 4} \quad (2.16)$$

where $\mathbf{0} = (0, 0, 0)^T$ is the null vector.

The transformation matrix \mathbf{T} therefore belongs to the Lie group $\mathbb{T} = (\mathbb{R}^+ \times SO(3) \times \mathbb{R}^3)$, and there is a corresponding vector space associated to \mathbb{T} , which is given by \mathfrak{t} . Given a $v = (l, \mathbf{A}, \mathbf{b}) \in \mathfrak{t}$, the exponential map is given by

$$\exp(l, \mathbf{A}, \mathbf{b}) = (e^l, e^{\mathbf{A}}, \mathbf{b}) \quad (2.17)$$

$$= (s, \mathbf{R}, \mathbf{b}) \quad (2.18)$$

Here, $e^{\mathbf{A}}$ is the matrix exponential of \mathbf{A} , and since $e^{\mathbf{A}} = \mathbf{R}$, \mathbf{A} is a skew-symmetric matrix defined as

$$\mathbf{A} = \begin{pmatrix} 0 & -\theta_z & \theta_y \\ \theta_z & 0 & -\theta_x \\ -\theta_y & \theta_x & 0 \end{pmatrix} \quad (2.19)$$

Therefore, for each surface, the pose can be represented as either the homogeneous transformation matrix \mathbf{T} , or a collection of the 7 independent parameters $(b_x, b_y, b_z, \theta_x, \theta_y, \theta_z, s)$, and these are both equivalent formulations and we will use them interchangeably.

For the population of surfaces $S^{(i)}$, the relative pose of each surface with respect to the Procrustes mean shape is calculated as the least-squares solution to the following cost

function

$$\mathbf{T}^{(i)} = \min_{\mathbf{T}} \left\| \mathbf{T}(\mathbf{V}^{(i)}) - \bar{\mathbf{V}} \right\|^2 \quad (2.20)$$

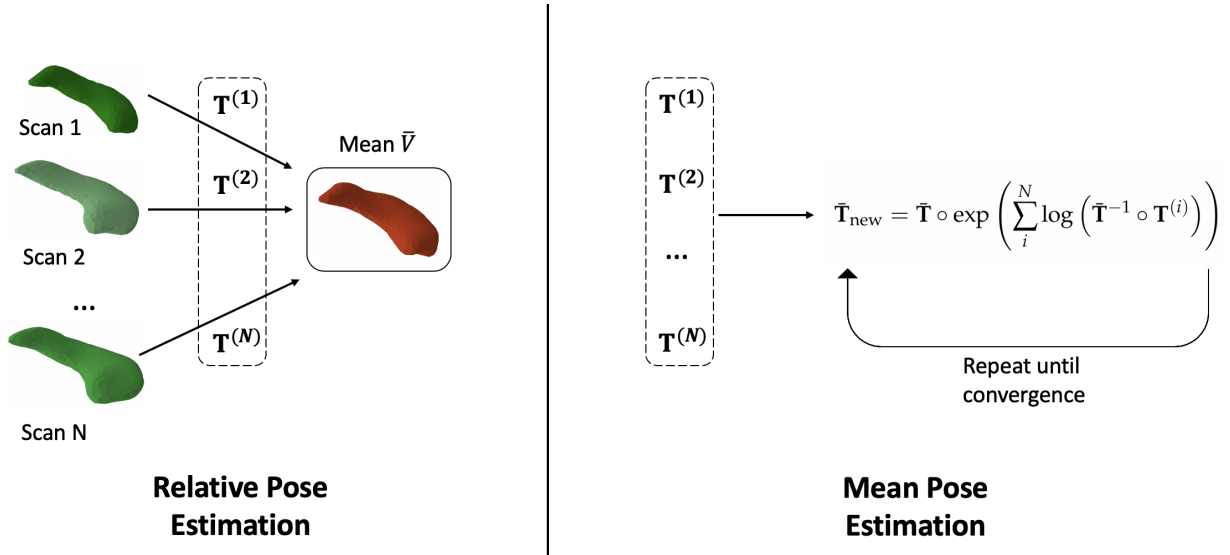


Figure 2.5: Procedures to calculate the relative poses (left), and the mean pose through an iterative procedure (right) upon obtaining the Procrustes mean shape for the population

2.6.1.3 Mean Pose Calculation

Using the Log-Euclidean framework, we can map the pose matrices $\mathbf{T}^{(i)}$ onto the vector space \mathfrak{t} , which allows us to use the addition and scalar multiplication operations defined on vector spaces to calculate a mean pose. The mean pose is calculated using the iterative

procedure described in Algorithm 2 (Pennec, Fillard, and Ayache, 2006) -

Algorithm 2: Algorithm to calculate the mean pose matrix

Data: $\mathbf{T}^{(i)} \in \mathbb{R}^{4 \times 4}$ for $i = 1, \dots, N$, $\bar{\mathbf{V}}$

Output: Mean pose $\bar{\mathbf{T}}$

Initialize mean pose as first pose matrix:

$\bar{\mathbf{T}} := \mathbf{T}^{(1)}$

while *not converged* **do**

 Calculate the new mean pose based on the individual poses :

$$\bar{\mathbf{T}}_{\text{new}} = \bar{\mathbf{T}} \circ \exp \left(\sum_i^N \log \left(\bar{\mathbf{T}}^{-1} \circ \mathbf{T}^{(i)} \right) \right) \quad (2.21)$$

if $\|\bar{\mathbf{T}}_{\text{new}} - \bar{\mathbf{T}}\| < \epsilon$ **then**

 | *converged*

else

 | $\bar{\mathbf{T}} := \bar{\mathbf{T}}_{\text{new}}$

end

end

2.6.1.4 Residual Pose Calculation

Upon obtaining the mean pose matrix, we can finally calculate the residual pose of each structure compared to the mean pose, by composing the pose matrix of each structure with the inverse of the mean pose matrix. This is equivalent to removing the mean pose transformation from the overall transformation of the structure, and can be written as

$$\mathbf{T}_r^{(i)} = \bar{\mathbf{T}}^{-1} \circ \mathbf{T}^{(i)} \quad (2.22)$$

$$= \begin{pmatrix} s^{(i)} \mathbf{R}^{(i)} & \mathbf{b}^{(i)} \\ \mathbf{0}^T & 1 \end{pmatrix} \quad (2.23)$$

The equivalent residual pose parameters $\mathbf{p}_r^{(i)}$ can be assembled by noting the below

1. Translation parameters are $\mathbf{b}^{(i)} = (b_x^{(i)}, b_y^{(i)}, b_z^{(i)})$
2. Scale parameter is $s^{(i)}$
3. The rotation matrix $\mathbf{R}^{(i)}$ can be decomposed into the equivalent Euler angle matrices

$\mathbf{R}_x^{(i)}$, $\mathbf{R}_y^{(i)}$, and $\mathbf{R}_z^{(i)}$, where each matrix can be written as

$$\mathbf{R}_x^{(i)} = \begin{pmatrix} 1 & 0 & 0 \\ 0 & \cos(\theta_x^{(i)}) & -\sin(\theta_x^{(i)}) \\ 0 & \sin(\theta_x^{(i)}) & \cos(\theta_x^{(i)}) \end{pmatrix} \quad (2.24)$$

and similarly for $\mathbf{R}_y^{(i)}$ and $\mathbf{R}_z^{(i)}$. The rotation parameters are then $(\theta_x^{(i)}, \theta_y^{(i)}, \theta_z^{(i)})$.

The residual pose for each structure is given by $\mathbf{p}^{(i)} = (s^{(i)}, b_x^{(i)}, b_y^{(i)}, b_z^{(i)}, \theta_x^{(i)}, \theta_y^{(i)}, \theta_z^{(i)})^T$.

2.6.2 Volume and Local Surface Analysis

Following restricted Delauney triangulation of the subcortical structures in question, shape analysis is performed for two different features: (1) the global volumes of the subcortical structures, and (2) local surface features on the surfaces of the subcortical structures.

Given a triangulated surface $\mathbb{S} = (\mathbf{V}, \mathbf{F})$ with N_V vertices where the j -th vertex has coordinates $(V_{j,x}, V_{j,y}, V_{j,z})$ with respect to the origin, the volume of the triangulated surface is calculated by summing over the volumes of the individual tetrahedrons that each triangle makes with the origin. For the i -th tetrahedron with coordinates $(\mathbf{0}, V_{1,:}, V_{2,:}, V_{3,:})$, the positive volume is given by the equation

$$\begin{aligned} v_{\text{tetrahedron}}^{(i)} = \frac{1}{6} & | -V_{3,x}V_{2,y}V_{1,z} + V_{2,x}V_{3,y}V_{1,z} + V_{3,x}V_{1,y}V_{2,z} \\ & - V_{1,x}V_{3,y}V_{2,z} - V_{2,x}V_{1,y}V_{3,z} + V_{1,x}V_{2,y}V_{3,z} | \end{aligned} \quad (2.25)$$

and therefore, the total area of surface \mathbb{S} with N_F triangulated faces is given by

$$v^{(i)} = \sum_{j=1}^{N_F} v_{\text{tetrahedron},j}^{(i)} \quad (2.26)$$

Similarly, we can also define a local surface feature by calculating the surface Jacobian of each vertex of a subcortical structure, which is defined as the ratio change of the area of the vertex in the scan with the area of the vertex in the surface template. The surface Jacobian

therefore gives us an idea of the amount of surface area that changes in each scan w.r.t the surface template.

The surface Jacobian of vertex j is obtained as follows

$$J_j = \frac{A_j^{(v)}}{A_{j,T}^{(v)}} \quad (2.27)$$

where $A_j^{(v)}$ is defined as the vertex area of vertex j , and $A_{j,T}^{(v)}$ is the vertex area of vertex j on the surface template of the subcortical structure. Vertex area in general is defined as

$$A_j^{(v)} = \sum_{k=1}^M A_{j,k} \quad (2.28)$$

where $A_{j,k}$ is the area of the k -th face consisting of vertex j , for a total of M faces that surround vertex j and consist of it.

2.7 Statistical Modelling

2.7.1 Cross-sectional Modelling

2.7.1.1 ANCOVA Analysis

For cross-sectional modelling of group difference between control subjects and subjects with strict schizophrenia, a general linear model known as the Analysis of covariance (ANCOVA) is used (Keppel, 1991), which evaluates whether the means of a dependent variable (DV) are equal across different levels of a categorical independent variable (IV), while statistically controlling for the effects of other continuous variables that are not of interest in the analysis, which are known as covariates (CV). ANCOVA analysis decomposes the variance in the DV across variance explained by the CV(s), variance explained by the categorical IV, and residual variance. The general linear model formulation of ANCOVA

analysis can be written as

$$y_{ij} = \mu + \tau_i + B(x_{ij} - \bar{x}) + \epsilon_{ij} \quad (2.29)$$

Here, the DV, y_{ij} is the j th observation in the i th categorical group; the CV, x_{ij} is the j th observation of the covariate under the i th group; μ is the grand mean of the observed data; and \bar{x} is the global mean for the covariate x . The fitting variables are τ_i , the effect of the i th categorical group, B , the slope of the line, and ϵ_{ij} , the associated unobserved error term for the j th observation in the i th group. The following assumptions are also considered to be true for the ANCOVA model

1. **Linearity of Regression:** The regression between the dependent variable and the covariates must be linear
2. **Homogeneity of error variances:** The error is considered to be a random variable with conditional zero mean and equal variances for different categories of the independent categorical variable.
3. **Independence of error terms:** The error terms are uncorrelated; or equivalently, the error covariance matrix is diagonal.
4. **Normality of error terms:** The error terms are normally distributed, which is to say that $\epsilon_{ij} \sim \mathcal{N}(0, \sigma^2)$
5. **Homogeneity of regression slopes:** The regression lines should be parallel across the two groups, and therefore the slopes of the regression lines is invariant across the categories of the independent variable.
6. The effects of the categorical groups τ_i sum to 0, which is to say $\sum_i \tau_i = 0$.

2.7.1.2 MANCOVA Analysis

A major restriction of ANCOVA analysis is the fact that there can only be a single dependent variable where the effects are modelled. However, it is easy to extend ANCOVA analysis to a multivariate analysis, which is known as Multivariate Analysis of Covariance (MANCOVA). In MANCOVA analysis, the goal is to test for significant difference between group means for the independent variable controlling for multiple covariate variables, and looking at more than one dependent variable. MANCOVA analysis also follows the same assumptions as ANCOVA analysis above (Davis, 2003).

2.7.2 Longitudinal Modelling

Both ANCOVA and MANCOVA analysis make a big assumption, which is the data has no longitudinal or time-series correlation, which is not accurate for the Schizconnect dataset, where there are subjects with multiple scans at different time-points. We can also model residual pose, volumetric and local surface changes across time in order to gauge a longitudinal progression of schizophrenia over time, in order to determine potential biomarkers of disease that manifest over the progression of the disease.

For longitudinal modelling of the data, we use a log-linear mixed effects model, in order to describe data involving multiple subjects, with multiple measurements per subject (Bates et al., 2014). We consider a model of the following form, looking to model a scalar-valued observation at each vertex on the triangulated surface, as

$$Y = X\beta + Zb + \epsilon \quad (2.30)$$

where Y is a $N \times 1$ vector of observations, X is a fixed effects design matrix, Z is a random effects design matrix, β are the fixed parameters and b are the random effects random variables, and ϵ is the noise. In this model, the individual terms have the following forms and assumptions:

1. We assume ϵ is independent and identically distributed (i.i.d) Gaussian with variance σ^2
2. We assume b is also i.i.d Gaussian with variance $\sigma^2\theta$. b will have one element per subject for a total of M subjects
3. Z is a binary matrix having one column per subject, with ones indicating which observations in Y come from that subject. Therefore, $Z \in \{0, 1\}^{N \times M}$.
4. Both X and β describe covariates such as age and gender (in our specific case)

By fitting this model to the data, the goal is to find maximum likelihood estimates of β, σ, θ , and the expected value of b .

2.7.3 Controlling for familywise error rate

One issue that pops up when performing multiple hypothesis tests at once (such as testing for significance at each vertex in a triangulated surface), is that the probability of seeing any false positives goes up, and we therefore need to correct for this error, which is known as the familywise error rate (FWER). We can formalize the FWER by looking at a collection of N statistics $H_i, i = 1, \dots, N$, and supposing that on the first N_0 of these statistics, the null hypothesis holds true. We define a rate of controlling the FWER a by choosing a test statistic threshold t , which translates to saying

$$P \left[\bigcup_{i=1}^{N_0} H_i \geq t \right] \leq a \quad (2.31)$$

For the purposes of this work, we look at two popular methods for controlling for the FWER, namely the Bonferroni correction, and permutation testing, both of which are described below

2.7.3.1 Bonferroni Correction

The most conservative approach to correcting for FWER is known as the Bonferroni correction, where we divide the usual threshold for statistical significance by N , the number of hypothesis tests performed (Dunn, 1961). To see why this corrects for FWER sufficiently, we can use the monotonicity of probability to show that

$$P \left[\bigcup_{i=1}^{N_0} H_i \geq t \right] \leq \sum_{i=1}^{N_0} P[H_i \geq t] \quad (2.32)$$

By choosing t such that each $P[H_i \geq t] \leq a/N$, we satisfy eq. 2.31.

2.7.3.2 Permutation Testing

In practise, the Bonferroni correction is very conservative and doesn't take into account dependence between random variables that affect the outcome of the statistical test, for example looking at vertices around the vertex the hypothesis test is being performed on. In order to achieve better statistical power, we look at properties of the maximum statistic. To motivate this, we observe that atleast one statistic is greater than the threshold t i.f.f the maximum statistic is greater than the threshold. Therefore,

$$P \left[\bigcup_{i=1}^{N_0} H_i \geq t \right] = P \left[\max_{i=1, \dots, N_0} H_i \geq t \right] \leq P \left[\max_{i=1, \dots, N} H_i \geq t \right] \quad (2.33)$$

One way of controlling the FWER then is by calculating the distribution of the maximum statistic, which can be done by resampling methods such as permutation testing (Nichols and Holmes, 2002; Tward, 2017b).

Supposing we have a random variable X and we observe x . Taking the group of transformations that are permutations \mathcal{P} , under the null hypothesis, the distribution of $\mathcal{P}_i X$ is the same as the distribution of X , where $\mathcal{P}_i \in \mathcal{P}$. Further, if we have a test statistic on X given by $H(X)$ with a rejection threshold t , we wish to control for the FWER under a ,

which translates to $P[H(X) \geq t] \leq a$. Considering the statistic

$$T(x) = \frac{1}{|\mathcal{P}|} \sum_i \mathcal{I}[H(\mathcal{P}_i x) \geq H(x)] \quad (2.34)$$

where \mathcal{I} is the indicator function, and $|\mathcal{P}|$ is the number of permutation transformations being considered. $T(x)$ is thus the proportion of times $H(\mathcal{P}_i x)$ was bigger than $H(x)$. It can be shown that, under the null hypothesis, the CDF of $T(x)$ is below the uniform CDF, which is to say

$$P[T(X) \leq u] \leq u \quad (2.35)$$

Further, it can be shown that if $H(X)$ is the maximum statistic, the FWER can be controlled at level a by choosing $1 - u \leq a$. Therefore, if we choose the threshold $u \geq 1 - a$, we can compute the original threshold t as the $1 - u$ -th quantile of $H(\mathcal{P}_i x)$.

For this study, in order to perform permutation testing to discriminate between a control and diseased group for some parameters, we use the family of permutations \mathcal{P} to rearrange the group labels across the dataset. For each permuted group \mathcal{P}_i , we calculate the maximum likelihood estimates for the mixed-effects model described in 2.7.2, and then compute a test statistic over all the vertices in the surface template, and then find $H(\mathcal{P}_i x)$ as the maximum over all the vertices.

Algorithm 1: Algorithm to calculate the Procrustes mean shape

Data: $\mathbf{V}^{(i)} \in \mathbb{R}^{N_V \times 3}$ for $i = 1, \dots, N$

Output: Mean structure $\bar{\mathbf{V}}$

Initialize mean as first structure:

$\bar{\mathbf{V}} := \mathbf{V}^{(1)}$

while *not converged* **do**

Center all structures to the origin by subtracting the mean of all vertex coordinates from each vertex:

$$\hat{\mathbf{V}}^{(i)} := \mathbf{V}^{(i)} - \frac{1}{N_V} \sum_{j=1}^{N_V} \mathbf{V}_{j:}^{(i)} \quad (2.10)$$

Normalize centered structures to have unit-norm by dividing each structure by its' L2-norm:

$$\check{\mathbf{V}}^{(i)} := \frac{\hat{\mathbf{V}}^{(i)}}{\|\hat{\mathbf{V}}^{(i)}\|} \text{ where } \|\check{\mathbf{V}}^{(i)}\| = 1 \quad (2.11)$$

Calculate the least-squares fit rotation matrix R_i that solves the following minimization equation:

$$\mathbf{R}^{(i)} := \min_{\mathbf{R}} \|\bar{\mathbf{V}} - \mathbf{R}\check{\mathbf{V}}^{(i)}\|^2 \quad (2.12)$$

The solution to above is given by $\mathbf{R}^{(i)} := \mathbf{W}\mathbf{U}^T$, where $\bar{\mathbf{V}}^T \check{\mathbf{V}}^{(i)} = \mathbf{U}\mathbf{\Sigma}\mathbf{W}^T$ is the singular-value decomposition.

Rotate each surface by this rotation matrix:

$$\tilde{\mathbf{V}}^{(i)} = \mathbf{R}^{(i)} \check{\mathbf{V}}^{(i)} \quad (2.13)$$

Calculate the new mean as the average of these centered, unit-normalized, and rotation-aligned surfaces:

$$\bar{\mathbf{V}}_{\text{new}} = \frac{1}{N} \sum_{i=1}^N \tilde{\mathbf{V}}^{(i)} \quad (2.14)$$

if $\|\bar{\mathbf{V}}_{\text{new}} - \bar{\mathbf{V}}\| < \epsilon$ **then**

| *converged*

else

| $\bar{\mathbf{V}} := \bar{\mathbf{V}}_{\text{new}}$

end

end

Chapter 3

Volumetric and Local Surface Analysis

3.1 Volume Regressions over Time

The first analysis we performed on the Schizconnect dataset involved modelling the volumes of both the binary segmentations and triangulated surfaces for 12 subcortical structures (6 structures with left and right hemispherical structures) as functions of time, in order to gain a better idea about the trend of volume change, as well as to ensure that this trend is preserved after the surface triangulation step of processing. The 6 subcortical structures considered here are the Amygdala, Hippocampus, Caudate nucleus, Putamen, Globus Pallidum, and Thalamus, with the left and right hemisphere structures totalling 12 independent structures.

From figures 3.1 and 3.2, we see that the volumes for binary segmentations don't exactly follow a monotonic downward trend, and there is significant variation in the distribution of volume change across subjects, for both controls and the diseased population. For all the subcortical structures under question, we notice that though there is an overall downward trend for volumes in subjects with exactly two scans, there are certain subjects where their subcortical volume tends to increase, which affects the overall volume change trend. For subjects with exactly 3 scans, even though a large number of subjects have a monotonic trend in volume (either increasing with time, or decreasing with time), there are subjects that do not follow this monotonic trend, which is not expected to be seen from

a biologically plausible perspective.

In order to smooth out variation that may arise from the binary segmentation performed by the MRICloud pipeline, we also look at volume trends for the triangulated surfaces, which are smoother approximations of the binary segmented subcortical structures. The Delauney triangulation process intrinsically smooths out the shapes of the subcortical structures, since we restrict the number of triangles that each surface can consist of. These volume trend plots are reported in figures 3.3 and 3.4. We can see, compared to the binary segmentation volumes, the volume trends here are much smoother and more monotonic, across all subcortical structures.

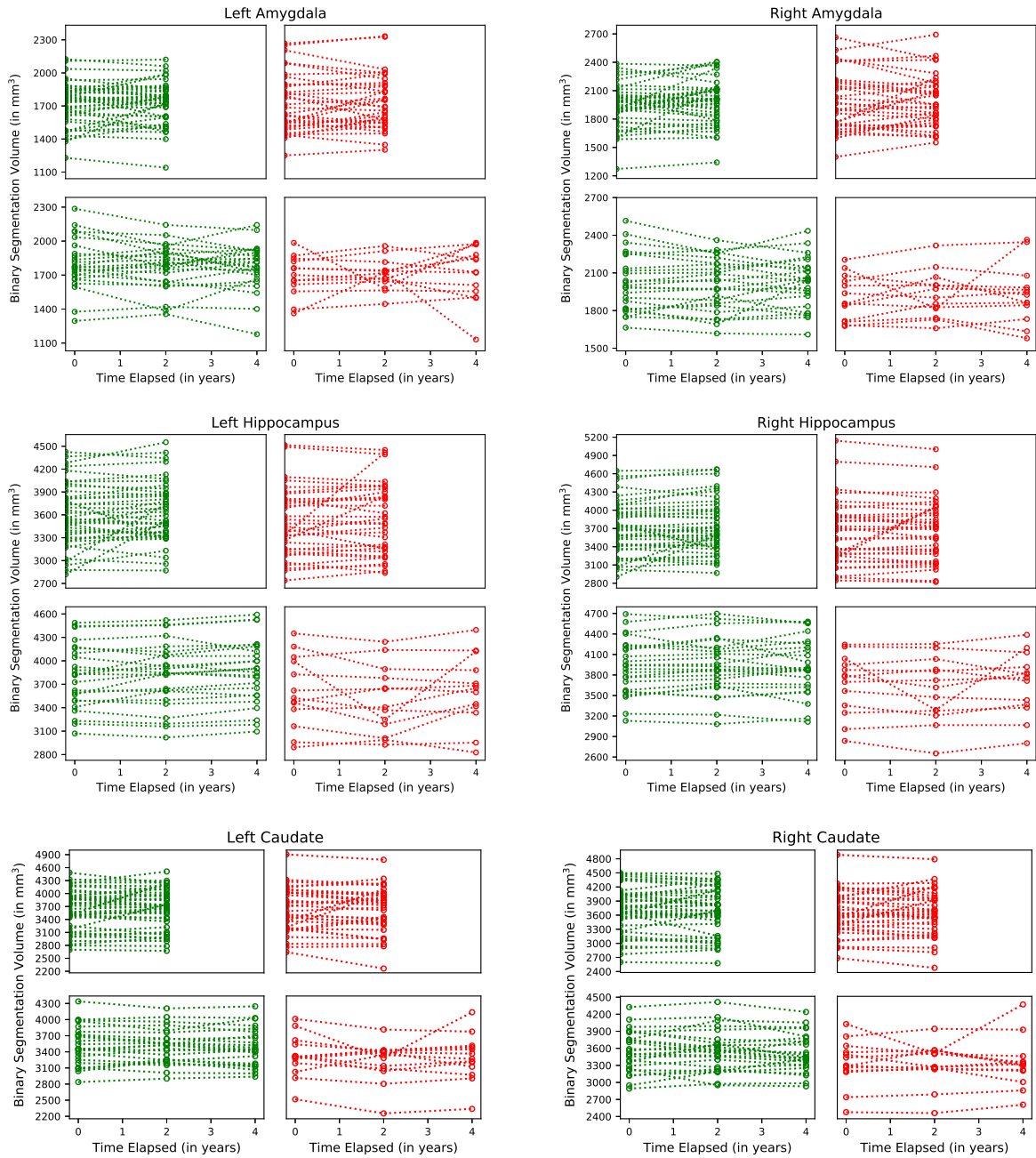


Figure 3.1: Line-plots of binary segmentation volumes for control subjects with 2 scans (top-left) and 3 scans (bottom-left), and diseased subjects with 2 scans (top-right) and 3 scans (bottom-right), for the Amygdala, Hippocampus, and Caudate.

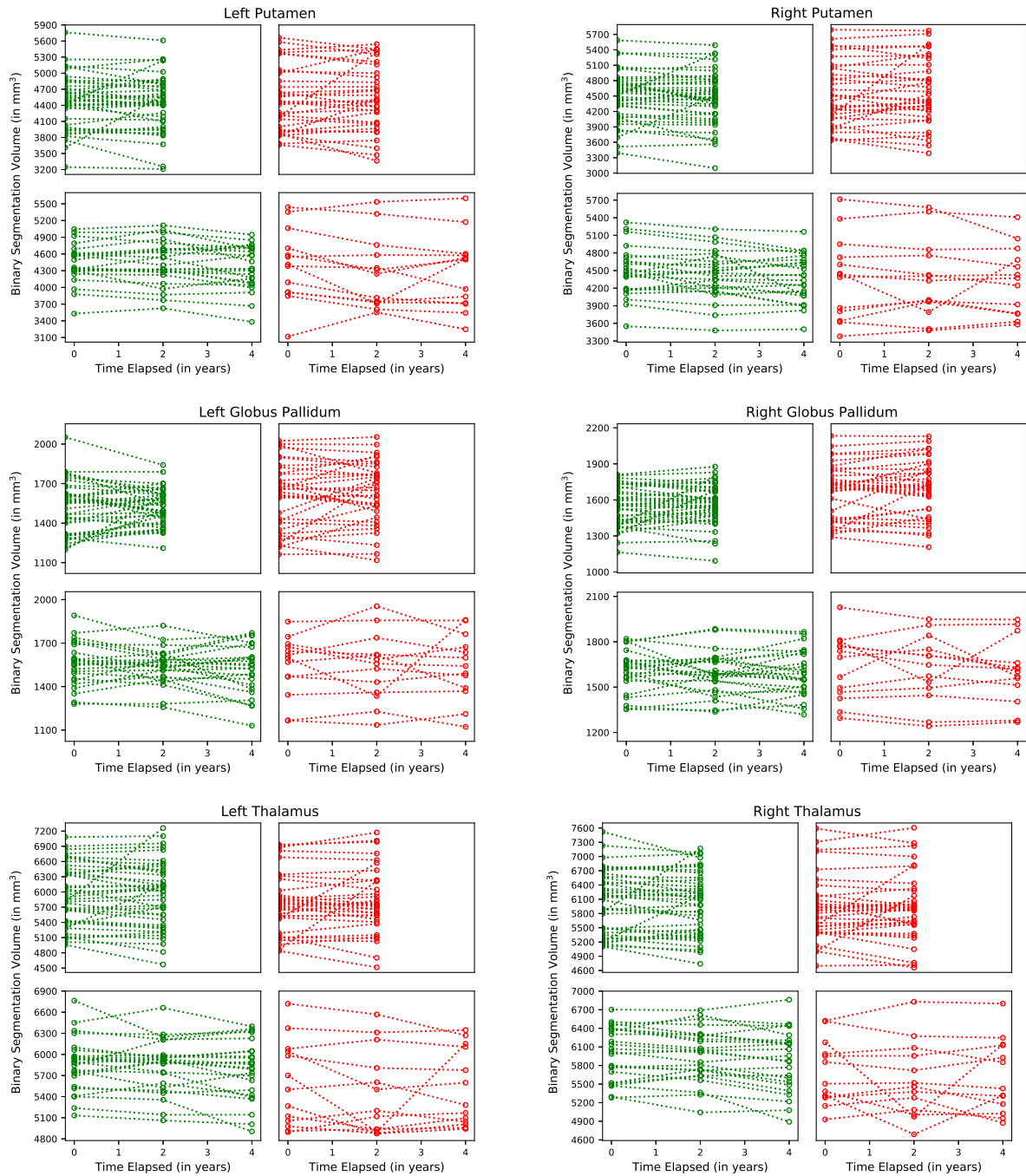


Figure 3.2: Line-plots of binary segmentation volumes for control subjects with 2 scans (top-left) and 3 scans (bottom-left), and diseased subjects with 2 scans (top-right) and 3 scans (bottom-right), for the Putamen, Globus Pallidum, and Thalamus.

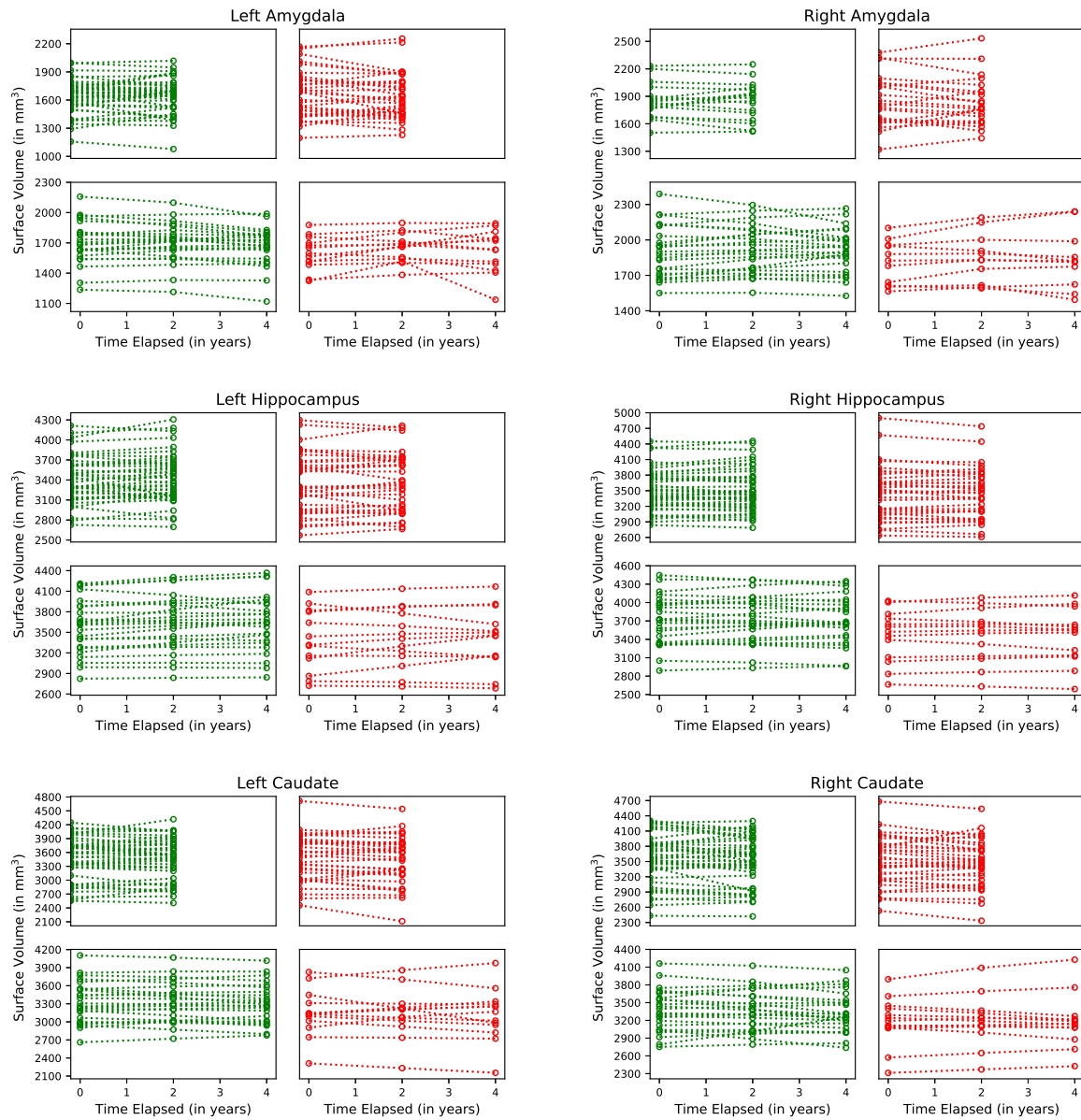


Figure 3.3: Line-plots of triangulated surface volumes for control subjects with 2 scans (top-left) and 3 scans (bottom-left), and diseased subjects with 2 scans (top-right) and 3 scans (bottom-right), for the Amygdala, Hippocampus, and Caudate.

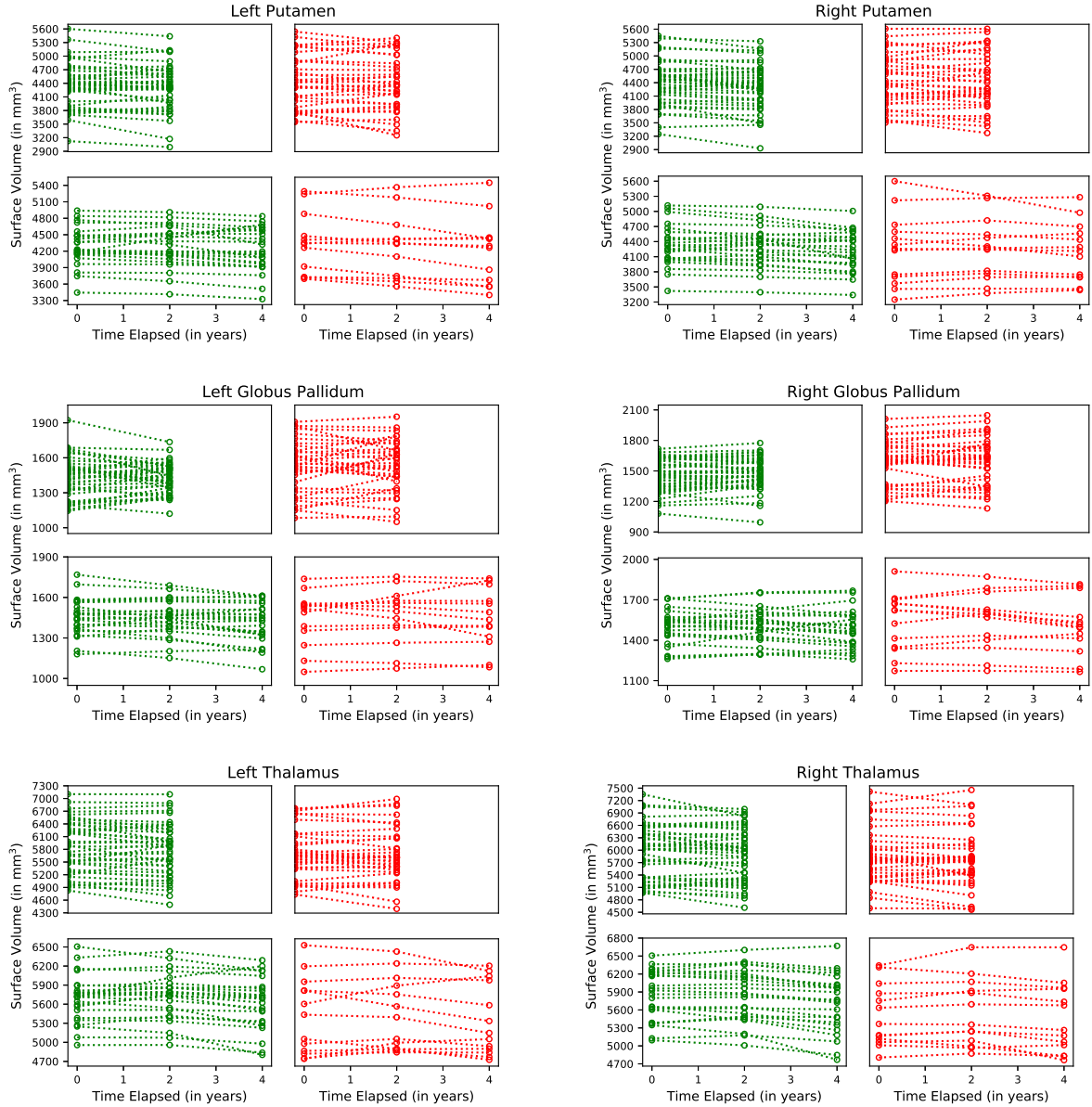


Figure 3.4: Line-plots of triangulated surface volumes for control subjects with 2 scans (top-left) and 3 scans (bottom-left), and diseased subjects with 2 scans (top-right) and 3 scans (bottom-right), for the Putamen, Globus Pallidum, and Thalamus

In order to further explore the distribution of volume slopes across the control and diseased populations, we calculate the best-fit lines for each subject's time-series data. Given a collection of subjects $i = 1, \dots, N$ with triangulated surface volumes $v_t^{(i)}$ for $t = 0, 2, \text{ or } 4$ years, we calculate the slopes of the best-fit lines. For subjects with exactly 2 scans, this is equal to the slope of the line between $v_0^{(i)}$ and $v_2^{(i)}$. For subjects with exactly

three scans, this is equal to the slope $m^{(i)}$ of the best-fit line that minimizes the least-squares error, which is given by

$$m^{(i)} = \frac{\sum_t (v_t^{(i)} - \bar{v}^{(i)})(t - \bar{t})}{\sum_t (v_t^{(i)} - \bar{v}^{(i)})^2} \quad t = 0, 2, 4 \text{ (in years)} \quad (3.1)$$

where $\bar{v}^{(i)}$ is the average of the volumes for subject i across their timepoints, and $\bar{t} = (0 + 2 + 4)/3 = 2$ (in years).

Given the collection of the slopes of the best-fit lines, we can look at the distribution of slopes across the control and diseased populations, and plot the histograms of slope-distributions, in order to have a better idea of the trend of volume change, which is seen in figures 3.5 and 3.6.

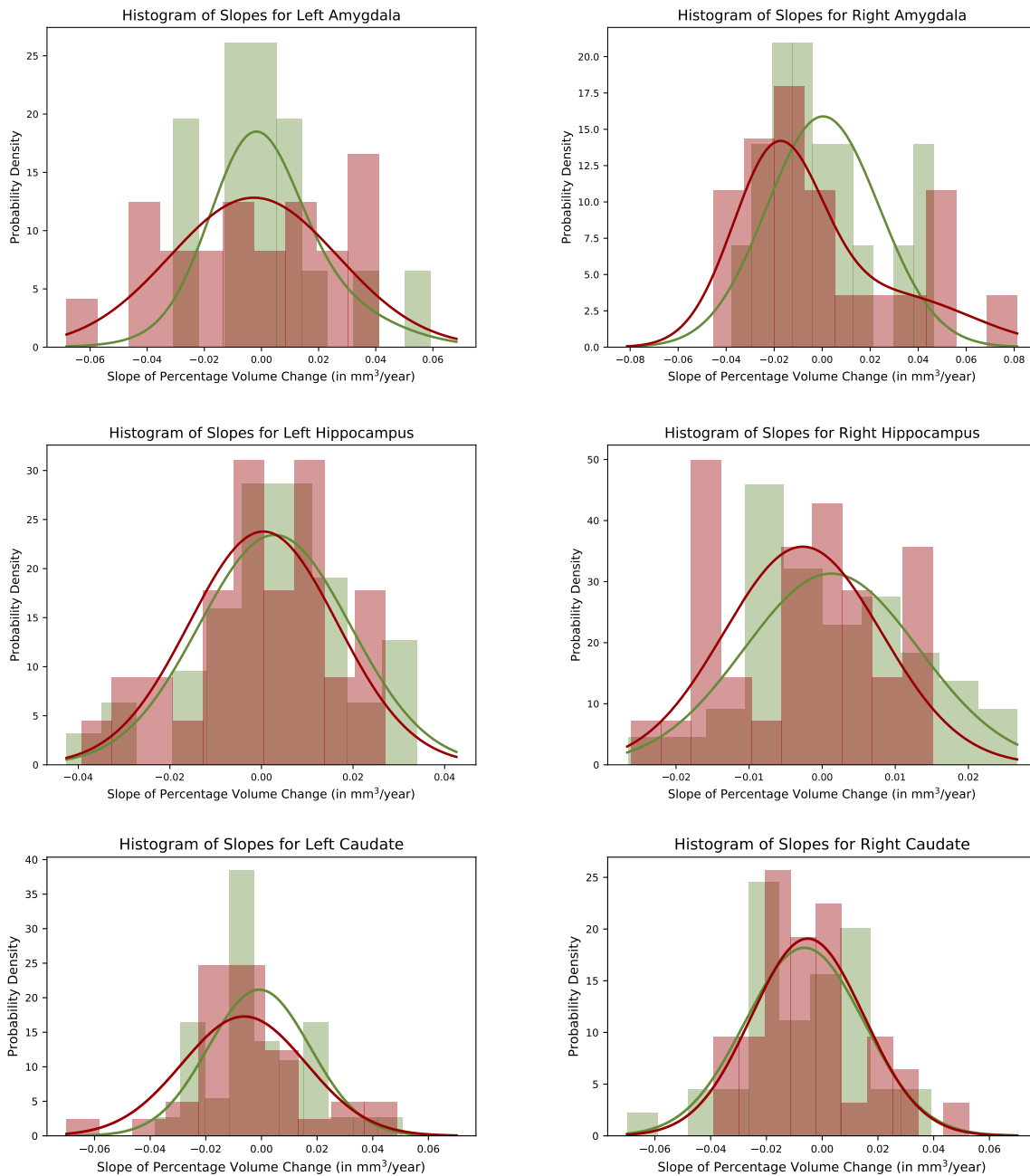


Figure 3.5: Histograms and best-fit probability distribution curves for volume slopes, for the Amygdala, Hippocampus, and Caudate. Green refers to the control group and red refers to the diseased group

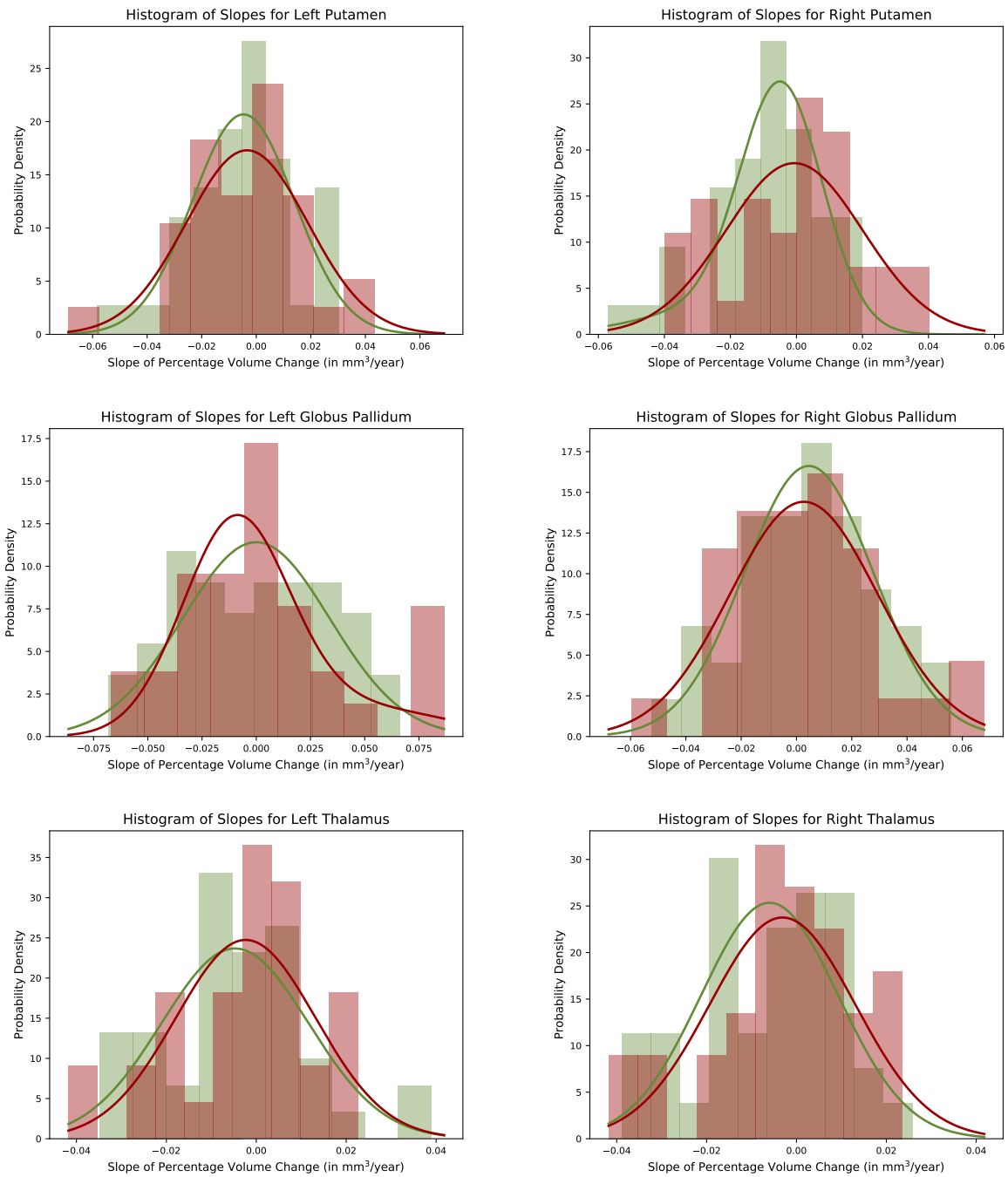


Figure 3.6: Histograms and best-fit probability distribution curves for volume slopes, for the Putamen, Globus Pallidum, and Thalamus. Green refers to the control group and red refers to the diseased group

From the histograms of slopes of percentage volume changes, we can see that there is a considerable distribution of subjects where their volume slopes are higher than zero,

for both controls and diseased groups. However, looking across all the subcortical structures, the mean slope of percentage volume slope is less than zero for most cases. For the amygdala, the slopes for diseased subjects are comparatively lower than the slopes for controls for the right structure, whereas for the left structure, the overall distributions look pretty similar, with the controls having a sharper distribution around smaller percentage change. For the hippocampus, the right structure has comparatively higher negative slopes for the diseased subjects compared to the controls, whereas the left structure has similar distributions. For the putamen, both the left and right structures seem to have slightly smaller negative slopes for the diseased subjects compared to the controls, implying lesser atrophy in the diseased subjects versus the controls. In the globus pallidum, for the left structure, the diseased subjects have comparatively higher negative slopes compared to the controls, whereas the distributions are similar for the right structure. For the thalamus, for both the left and right structures, the diseased subjects showed a trend to have smaller negative slopes, and even slightly positive slopes compared to the controls, implying either smaller atrophy or even a net positive volume increase over time for the diseased population.

Based on the preliminary analysis performed in section 3.1, we conclude that the distribution of slopes for volume change vary considerably across the dataset, which makes it difficult to conclude a relevant trend of different atrophy or volume change based on line regressions alone. In order to further probe group differences for subcortical structure volumes, and take into account various biases that may pop up in analyses on line regressions, we perform both cross-sectional and longitudinal analysis in the following sections

3.2 Volumetric and Local Surface Analysis

3.2.1 Longitudinal modelling with mixed-effects models

To carry out an unbiased longitudinal modelling for both subcortical volumes and surface Jacobians over time for subjects in the Schizconnect dataset, we use the mixed-effects model described in subsection 2.7.2.

Given a subject i with a scan at time-point j , the volume of the triangulated surface for a specific subcortical structure is estimated as $v_j^{(i)}$. If the surface template for the corresponding subcortical structure is given as $\mathbb{S}_T = (\mathbf{V}_T, \mathbf{F}_T)$, where $\mathbf{V}_T \in \mathbb{R}^{N_V \times 3}$, then the surface Jacobians calculated for subject i with a scan at time-point j is given by $\mathbf{J}_j^{(i)}$, with $\mathbf{J}_j^{(i)} \in \mathbb{R}^{N_V \times 1}$. The mixed-effects model for modelling the subcortical volumes is

$$\begin{aligned} \log(v_j^{(i)}) &= a_0 + a_1 \left(\text{elapsed time}_j^{(i)} \right) + b_0 \left(\text{age}^{(i)} \right) + b_1 \left(\text{gender}^{(i)} \right) \\ &+ \text{group label}^{(i)} \left[a_2 + a_3 \left(\text{elapsed time}_j^{(i)} \right) \right] + e^{(i)} + \epsilon_j^{(i)} \end{aligned} \quad (3.2)$$

Here, the null hypothesis is that the group of the subjects are interchangeable. Formally,

Null hypothesis $H^{(0)}$: group is interchangeable

$$: a_2 = a_3 = 0$$

Alternate hypothesis $H^{(A)}$: group is not interchangeable

$$: a_2 \neq 0, a_3 \neq 0$$

Similarly, a mixed-effects model is defined for each vertex in the surface template that has one-to-one correspondence across the subjects and scans. For a surface template \mathbb{S}_T with N_V vertices, there will be a total of N_V models, where for each vertex $k = 1, \dots, N_V$, the

model is defined as follows

$$\begin{aligned} \log \left(\mathbf{J}_{j,k}^{(i)} \right) &= a_{0,k} + a_{1,k} \left(\text{elapsed time}_j^{(i)} \right) + b_{0,k} \left(\text{age}^{(i)} \right) + b_{1,k} \left(\text{gender}^{(i)} \right) \\ &+ \text{group label}^{(i)} \left[a_{2,k} + a_{3,k} \left(\text{elapsed time}_j^{(i)} \right) \right] + e_k^{(i)} + \epsilon_{j,k}^{(i)} \end{aligned} \quad (3.3)$$

where the hypotheses for each vertex k are formalized as

Null hypothesis $H_k^{(0)}$: group is interchangeable for vertex k

$$: a_{2,k} = a_{3,k} = 0$$

Alternate hypothesis $H_k^{(A)}$: group isn't interchangeable for vertex k

$$: a_{2,k} \neq 0, a_{3,k} \neq 0$$

The effective significance for surface Jacobian differences across the two groups is reported by taking the maximum statistic over the N_V vertices in the surface template for a sub-cortical structure. In order to correct for the FWER, we perform permutation testing by permuting the group labels for the dataset 20000 times. In these 20000 permutations, if the test statistic is higher for a permuted group compared to the actual labels more than 1000 times, we declare the group label being statistically significant ($p < 0.05$). Permutation testing and mixed-effects modelling is performed for both paradigms of surface template estimation: (1) Unique STEs for the left and right hemispheres, and (2) Combined STEs, and these results are reported in tables below

Subcortical Structure	w/ Unique STE			w/ Combined STE		
	<i>p</i> -value (Volumes)	<i>p</i> -value (s. Jac.)	% of significant vertices	<i>p</i> -value (Volumes)	<i>p</i> -value (s. Jac.)	% of significant vertices
Amyg L	0.10	0.295	11.89 %	0.385	0.780	0.88 %
Amyg R	0.45	0.167	7.46 %			
Hippo L	0.02	0.536	11.95 %	0.016	0.049	28.21 %
Hippo R	0.04	0.224	12.47 %			
Caud L	0.08	0.584	1.99 %	0.88	0.6015	1.8 %
Caud R	0.32	0.1535	7.37 %			
Put L	0.95	0.7605	1.221 %	0.987	0.9465	0.00 %
Put R	0.30	0.8480	1.901 %			
GP L	0.29	0.1770	7.149 %	0.2908	0.13	13.63 %
GP R	0.37	0.2260	11.055 %			
Thalamus L	0.10	0.1940	3.074 %	0.0486	0.220	18.89 %
Thalamus R	0.04	0.1220	9.7808 %			

Table 3.1: Significance values for mixed-effects modelling of log(volume) and log(surface Jacobians) and percentage ratios of significant vertices, for both unique STEs for left and right hemispheres (left), and combined STEs (right). *p*-values below 0.05 are reported in bold

From table 3.1 we can see that of all the subcortical structures, only the hippocampus and thalamus show statistically significant changes in longitudinal modelling of subcortical volumes. Comparing the longitudinal models with the two paradigms of surface template estimates, we can see that there is correlation between the subcortical structures that show statistical significance when mapped to the unique templates, and when mapped to the combined template. Both the hippocampus and thalamus have statistically significant differences in volume across the controls and diseased population, for both the unique STE model and the combined STE model. We can also see that none of the other subcortical structures show significantly different volumes.

For the amygdala, we see that volume doesn't vary significantly for either of the two paradigms, however both the left and right amygdalas, there is a good proportion of vertices that are significant in terms of surface Jacobian difference. From figure 3.7, we

can see these regions plotted on the left and right surface templates, and we can see that these vertices form contiguous regions. However, on performing the same analysis with the combined STE, we don't see any vertices with significantly different surface Jacobian values, and one reason for this could be that across the left and right hemispheres of the amygdala, the same spatial regions are not significant. Since the combined surface template flips all right volumes and then performs diffeomorphic mapping with the surface template, there is an implicit symmetry between vertices on the left and right volumes that is being mapped. Since the regions of significance don't occur in the same spatially corresponding regions across the left and right volumes, we can conclude that the regions of possible atrophy in the amygdala are asymmetric across the left and right hemispheres. However, there is also a possibility that the effect size of significance in the unique STE paradigm is small, and is removed when considering a larger number of vertices in the combined STE paradigm.

For the hippocampus, both the left and right volumes are significantly different in terms of volume for the unique and combined STE paradigms. We notice that for the individual hemispheres, the surface Jacobians are not statistically significant, but for the combined STE, there are a much larger percentage of vertices that show p -values below 0.05, and the maximum statistic for the combined surface template is statistically significant as well. One way of interpreting this discrepancy across the two STE paradigms is that there are a lot of common vertices across the left and right hemispheres that have similar surface Jacobians, and upon performing a statistical analysis on the combined ST, we can see this, as well as from the plots in figure 3.7, where the tail of the hippocampus has regions of significant surface Jacobian differences across the two groups for the left, right and the combined surface templates.

For the caudate and putamen, across both paradigms of STE, we don't see any statistical

significance for either the volumes or the surface Jacobians. For the right caudate, there is a significant proportion of vertices with p -values below 0.05, however this does not translate to significance on the combined STE, implying that this is asymmetric significance in the right caudate over the left caudate. For the putamen, there are very few vertices with statistical significance in either of the two STE paradigms.

The globus pallidum also does not show any statistically significant differences across the two groups, however for the vertex surface Jacobian values, there is a significant region of difference, which can also be seen from figure 3.8, where the combined ST shows both the regions seen on the left ST and the right ST, implying that both these regions are affected across the hemispheres.

Finally, the thalamus shows statistically significant volumes for the right volume, as well as for the combined ST. There are also regions of vertices with statistically significant surface Jacobians, especially in the combined ST, implying that there is potentially significant symmetric local surface changes across the left and right thalamus surfaces.

Given the mixed-effects models described by equations 3.2 and 3.3, we can also calculate global atrophy rates for the subcortical structures. For each subcortical structure, looking at the fit mixed-effects model, the global atrophy rate in percentage per year for the two groups, control (0) and diseased (1) is given as

$$\gamma = 100(1 - e^{a_1 + a_3(\text{group label})}) \quad (3.4)$$

Similarly, for each of the mixed-effects models fit to the surface Jacobians at the vertices, we can calculate local atrophy rates in percentage per year at the vertices as the following

$$\gamma_k = 100(1 - e^{a_{1,k} + a_{3,k}(\text{group label})}) \quad (3.5)$$

For each of the mixed-effects models that were fit using maximum-likelihood estimation above, we report the corresponding global atrophy rates for both the control and diseased groups, for both the unique STE and combined STE paradigms in table 3.2

Subcortical Structure	w/ Unique STE		w/ Combined STE	
	Atrophy Rate in Controls (%)	Atrophy Rate in Disease (%)	Atrophy Rate in Controls (%)	Atrophy Rate in Disease (%)
Amyg L	0.60	-0.14	0.0117	0.088
Amyg R	0.56	0.15		
Hippo L	-0.41	-0.06	-0.227	-0.046
Hippo R	-0.03	0.12		
Caud L	0.08	0.68	0.1125	0.2241
Caud R	0.77	0.22		
Put L	0.52	0.60	0.520	0.536
Put R	0.65	0.20		
GP L	1.04	-0.11	0.264	0.027
GP R	0.28	0.26		
Thalamus L	0.48	0.31	0.446	0.357
Thalamus R	0.81	0.34		

Table 3.2: Atrophy Rates for the Control and Disease groups in % per year for subcortical structures for both unique STEs for the left and right hemispheres (left), and combined STEs (right)

From table 3.2 we can see that for most subcortical structures, across the left and right hemispheres, there is positive global atrophy rate, which corresponds to a reduction in volume across the longitudinal scans. However, looking at global atrophy rates in the unique STE paradigm, we can see that there are cases of obtaining negative atrophy rate, which corresponds to an increase in volume. For example, in the diseased group for the left amygdala, left hippocampus, and the left globus pallidum, and for the left and right hippocampi for the control group. There are a few possible explanations for seeing negative atrophy rates that suggest an increase in volume with time. There have been studies that have shown an increase in volume for the globus pallidum and putamen for schizophrenic patients (Ellison-Wright and Bullmore, 2010). At the same time, we also see increasing volumes for the hippocampi for both the controls and the diseased groups,

which does not correspond to any known clinical results seen before in the literature, and we discuss this phenomenon further in the discussion section. Due to irregularities in the binary segmentations themselves, and as observed from the volume regression plots, there are subjects that exist in both the control and diseased groups that have subcortical structures that increase in volume with time, and we believe that this may partially be a result of suboptimal preprocessing of the data and triangulation of the binary segmentations. At the same time, negative atrophy rates (corresponding to increasing volume with time) could also reflect other factors such as subject misidentification, effects of scanner noise, or subject movement in the scanner, amongst other confounding effects. For this reason, we look at results for global atrophy with respect to the combined STE paradigm, as generating a surface template from both left and right hemisphere volumes tended to smooth out the surface template, and remove some variation in the noise that may affect the quality of unbiased diffeomorphic mapping. Looking at table 3.2 for the combined STE paradigm, we see that only the hippocampi report negative global atrophy rates (which correspond to an increase in subcortical volume), whereas the other subcortical structures report positive global atrophy rates. The caudate, putamen, and hippocampus report higher volume atrophy for the diseased group versus the control group, whereas the amygdala, globus pallidum, and thalamus report higher volume atrophy for the control group versus the diseased group.

Figures 3.7 and 3.8 show triangulated mesh plots of the surface templates for the subcortical structures under question, with the p -values plotted at each vertex. For vertices with p -values greater than 0.05, we set the plotted values to 0.05 (shown in yellow), and for statistically significant vertices, we plot the p -values from 0.05 (yellow) to 0 (blue).

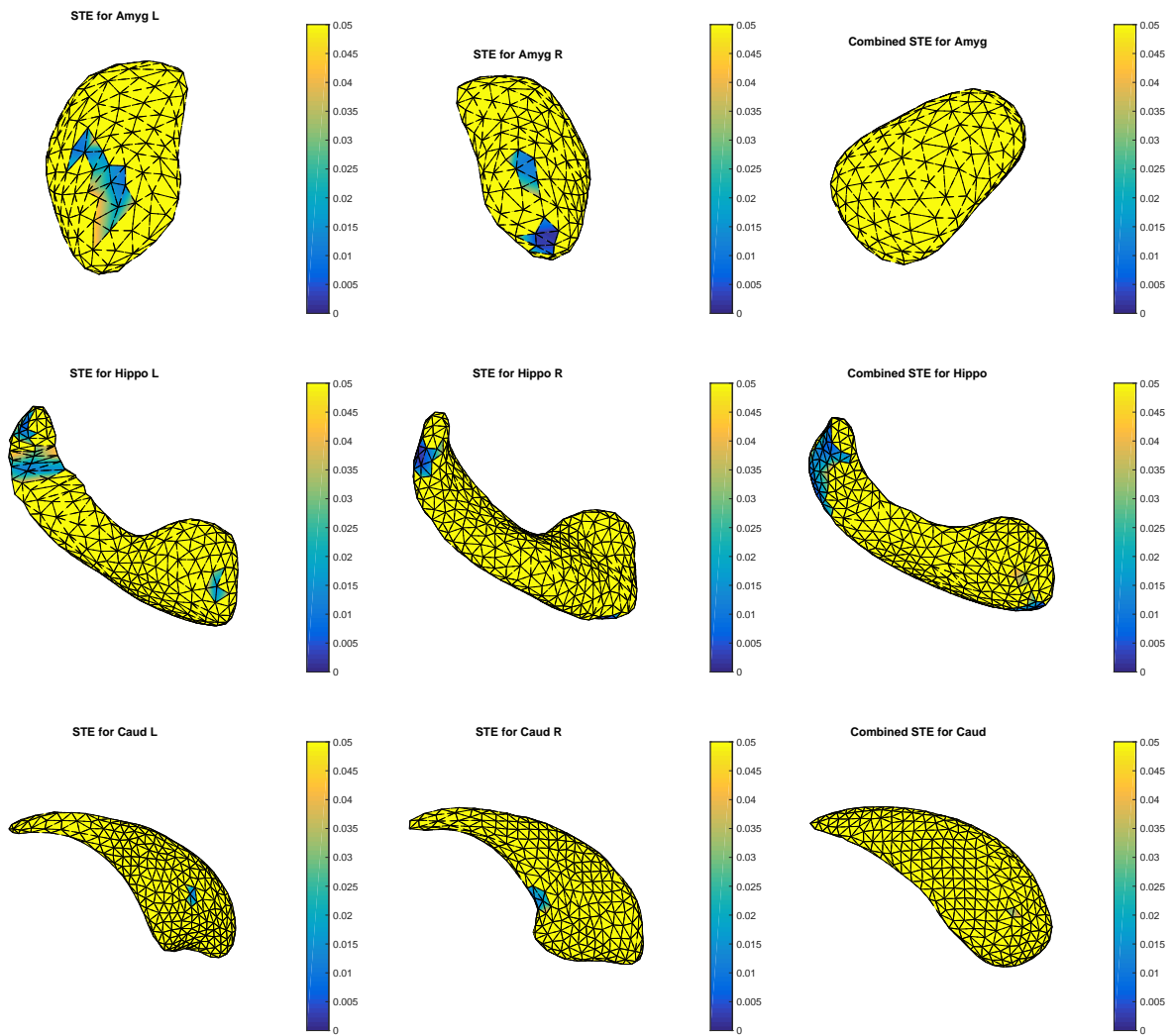


Figure 3.7: Surface p -value plots showing statistically significant vertices for the left surface template (left), the right surface template (center), and the combined surface template (right); for the Amygdala, Hippocampus, and Caudate

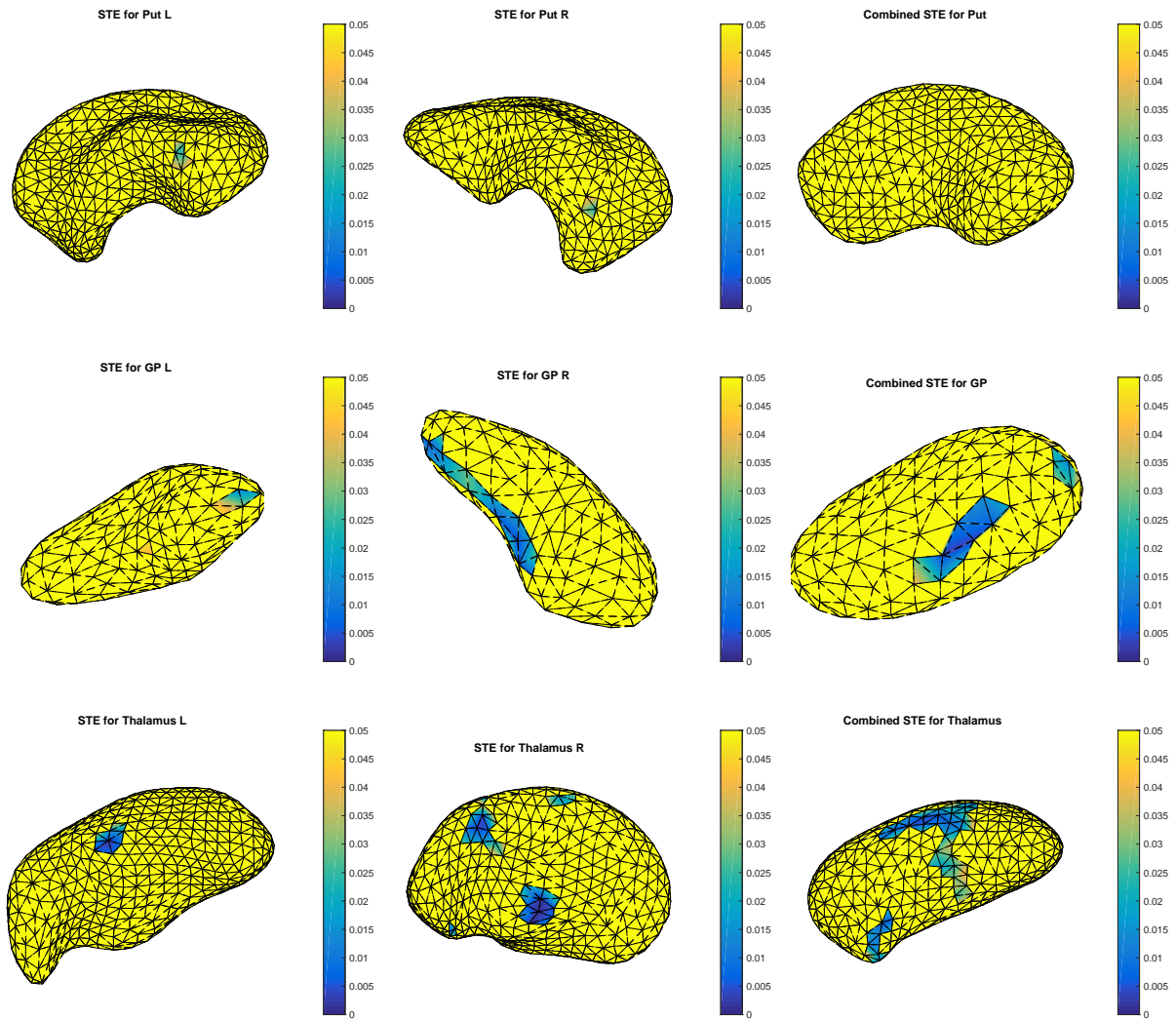


Figure 3.8: Surface p -value plots showing statistically significant vertices for the left surface template (left), the right surface template (center), and the combined surface template (right); for the Putamen, Globus Pallidum, and Thalamus

Chapter 4

Residual Pose Analysis

4.1 Residual Pose analysis

Following the volumetric and local surface analysis, and based on studies showing that the residual pose of subcortical structures can capture complementary information to shape, we perform residual pose analysis on 6 subcortical structures, motivated by the methods and algorithms described in subsection 2.6.1. After calculating a mean structure using generalized orthogonal Procrustes analysis, the pose transformation matrices (or pose matrices) are calculated that map each subcortical structure to the mean structure. The mean transformation matrix (or mean pose) is calculated across the population (Pennec, Fillard, and Ayache, 2006), which is then subtracted from each individual pose matrix to obtain the residual pose. Finally, using the decomposition steps described in equations 2.22 and 2.24, we obtain the residual pose features for each scan in the dataset, given by $\mathbf{p}^{(i)} = (s^{(i)}, b_x^{(i)}, b_y^{(i)}, b_z^{(i)}, \theta_x^{(i)}, \theta_y^{(i)}, \theta_z^{(i)})^T$. In the following subsections, we broadly perform cross-sectional and longitudinal modelling of statistical differences across the pose parameters $\mathbf{p}^{(i)}$, further details of which are described below

4.1.1 Cross-sectional Analysis

Based on the results seen in chapter 3, we decided to perform a cross-sectional analysis on the baseline scans for each subject within the Schizconnect dataset, ignoring scans that occurred at later time-points and only keeping scans that occurred at $t = 0$. The reasoning for this was to see if, across the cross-sectional population, there were statistically significant differences between the two groups without considering the longitudinal nature of the data, in order to avoid biasing the cross-sectional analysis by subjects that may have volume trends that are not necessarily clinically justified, and may be due to preprocessing artifacts and other issues discussed in the discussion. Table 4.1 reports the p -values for cross-sectional analysis of residual pose parameters for four different statistical tests, across the 12 subcortical structures (left and right hemispheres were considered independent). These 4 statistical tests were

1. Univariate test for scale parameter s , using ANCOVA analysis
2. Multivariate test for rotation parameters $(\theta_x, \theta_y, \theta_z)$, using MANCOVA analysis
3. Multivariate test for translation parameters (b_x, b_y, b_z) , using MANCOVA analysis
4. Multivariate test for all 7 parameters, using MANCOVA analysis

Also, since we perform 4 comparisons for 12 subcortical structures, we use the Bonferroni correction to control for the FWER, and therefore a p -value of less than $0.05/(4 \times 12) = 0.00104$ is considered statistically significant. We report these results for the 12 subcortical structures in the unique STE paradigm in Table 4.1.

Subcortical Structure	s	$(\theta_x, \theta_y, \theta_z)$	(b_x, b_y, b_z)	All 7 parameters
Amyg L	0.000667	0.058000	0.411000	0.120000
Amyg R	0.022804	0.892000	0.000001	0.000014
Hippo L	0.000249	0.071504	0.002394	0.002632
Hippo R	0.000830	0.008528	0.362530	0.102553
Caud L	0.030448	0.194213	0.502452	0.548150
Caud R	0.000076	0.051955	0.044050	0.005975
Put L	0.337230	0.209975	0.015170	0.002111
Put R	0.985837	0.001597	0.262407	0.001445
GP L	0.450223	0.002870	0.014281	0.000063
GP R	0.481363	0.000007	0.001517	0.000027
Thalamus L	0.000196	0.381065	0.082443	0.048614
Thalamus R	0.001689	0.008407	0.972245	0.011869

Table 4.1: Significance values for cross-sectional analysis for residual pose parameters p_i . Statistically significant pose parameters are reported in bold.

From this table, we can see that there are some similarities in significance compared to volumetric mixed-effects modelling, and some differences as well.

For the amygdala, we see that compared to no statistical significance being observed in volumetric analysis, here the left amygdala has significantly different scale between the diseased and controls, and the right amygdala has significantly different translation between the two groups, as well as a significantly different global pose. These results imply that the right amygdala is spatially shifted between the two groups even if there aren't significant volume changes between the groups, which could point to disease-specific affects in the regions immediately surrounding the right amygdala. At the same time, the left amygdala does show significantly different scale, which is a rough correlator of volumetric difference as well.

For the hippocampi, we see that both the left and right hippocampus are statistically different in their scales between the control and diseased groups, which corresponds very well with the volumetric differences we had seen in the longitudinal volumetric and local surface analysis as well, as amongst the 7 residual pose parameters, scale corresponds the most with volumetric change, as a tendency to have higher atrophy in one group over the other would correspond to that group have a relatively smaller scale compared to the other.

For the caudate and putamen, similar to our previous analysis, we do not see statistically significant differences in the residual pose parameters across the two groups, except for a scale difference in the right caudate. For the globus pallidum, we can see that there are significant differences in the global residual pose, while at the same time the scale parameters are not significant in the univariate analysis. This correlates well with the volumetric analysis where we did not see any significant differences in both volume and local surface changes. However, the fact that globus pallidum has significant global pose differences points to the fact that both the translation and rotation effects also play a role in statistically different changes across the control and diseased groups, and this is complementary information to what can be detected by volumetric analysis alone.

Finally, for the thalamus, we only see a scale difference in the left thalamus, which very roughly corresponds to the volumetric differences seen in the thalamus in chapter 3. From the cross-sectional analysis here, we can see that not only do we get results that correspond to volumetric analysis, but at the same time, for the amygdala and globus pallidum, we get complementary information in the form of the rotation and translation vectors of the residual pose parameters, which cannot be directly captured using volumetric or local surface information. It is important to note that though scale parameters are closely linked to volumetric features as well, they do not have a one-to-one correspondence, as scale only models a global rigid transformation in the same shape across two groups, whereas

differences in volume exist for similar structures that have different shapes as well.

4.1.2 Longitudinal Analysis

Further, we fit a mixed-effects model similar to the volumetric analysis for the residual pose parameters as well, defined as

$$\begin{aligned} \log \left(\mathbf{p}_{j,k}^{(i)} \right) = & a_{0,k} + a_{1,k} \left(\text{elapsed time}_j^{(i)} \right) + b_{0,k} \left(\text{age}^{(i)} \right) + b_{1,k} \left(\text{gender}^{(i)} \right) \\ & + \text{group label}^{(i)} \left[a_{2,k} + a_{3,k} \left(\text{elapsed time}_j^{(i)} \right) \right] + e_k^{(i)} + \epsilon_{j,k}^{(i)} \end{aligned} \quad (4.1)$$

for $k = 1, \dots, 7$. These results are reported below for both the unique STE and the combined STE paradigms

Subcortical Structure	x	y	z	θ_x	θ_y	θ_z	s	P_{total}
Amyg L	0.35	0.44	0.55	0.22	0.39	0.53	0.06	0.13
Amyg R	0.76	0.15	0.03	0.67	0.60	0.28	0.35	0.19
Hippo L	0.66	0.01	0.73	0.75	0.13	0.76	0.09	0.11
Hippo R	0.45	0.87	0.54	0.67	0.11	0.86	0.20	0.59
Caud L	0.76	0.45	0.02	0.15	0.05	0.79	0.01	0.02
Caud R	0.43	0.58	0.17	0.88	0.78	0.21	0.04	0.07
Put L	0.58	0.10	0.41	0.79	0.79	0.43	0.95	0.54
Put R	0.90	0.06	0.92	0.51	0.99	0.18	0.59	0.53
GP L	0.67	0.38	0.20	0.14	0.09	0.23	0.55	0.46
GP R	0.15	0.57	0.70	0.07	0.08	0.17	0.82	0.41
Thalamus L	0.38	0.25	0.09	0.73	0.40	0.06	0.10	0.25
Thalamus R	0.36	0.53	0.95	0.89	0.11	0.24	0.08	0.22

Table 4.2: Significance values for longitudinal mixed-effects modelling of residual pose parameters for the unique STE paradigm for left and right hemisphere

Subcortical Structure	x	y	z	θ_x	θ_y	θ_z	s	P_{total}
Amyg	0.5405	0.8020	0.3950	0.0495	0.8890	0.7040	0.3610	0.3730
Hippo	0.4379	0.6423	0.6157	0.4225	0.0041	0.1981	0.0420	0.0246
Caud	0.1960	0.5805	0.5545	0.1850	0.8570	0.0170	0.6430	0.2205
Put	0.4283	0.7721	0.8772	0.7233	0.5443	0.5281	0.8629	0.9826
GP	0.5315	0.2170	0.7355	0.1367	0.6203	0.4506	0.9184	0.5835
Thalamus	0.7576	0.1759	0.0834	0.9434	0.8866	0.3957	0.2236	0.4598

Table 4.3: Significance values for longitudinal mixed-effects modelling of residual pose parameters for the combined STE paradigm

From tables 4.2 and 4.3 we can see that upon fitting mixed-effects models to residual pose parameters, we lose a lot of the statistical significance that we have seen in the previous analyses. For the unique STE paradigms, only the caudate is consistently significant in terms of the scale parameter, and only the left caudate has globally significant residual pose. The right amygdala and the left hippocampus have statistically different translation parameters, in the z and x dimensions respectively. It is interesting to note that the structures that were significant in the cross-sectional analysis are no longer significant when modelled by a mixed-effects model, and we discuss this further in the discussion. One possibility that we attempt to remedy is the possibility that due to irregular binary segmentation, the longitudinal mapping is not optimal, and therefore we also run the longitudinal analysis with the combined SET paradigm.

We can see that there is not a lot of correlation between subcortical structures showing similar statistical significance across the unique and the combined STE paradigms. For example, on treating the left and right amygdalas independently, only the right amygdala shows significance in the z -direction, however in the combined STE paradigm, the amygdala only shows significance in the θ_x variable. Similarly, in the unique STE paradigm, the left hippocampus varies significantly in the translation along the y -direction, however the hippocampus combined across the left and right hemispheres shows statistical significance

across the θ_y direction, and the scale parameter, which agrees well with both the pose cross-sectional analysis, and the volumetric and local surface analysis. For the caudate, by combining the left and right volumes, we lose the global pose significances, which could be due to a lot of the statistical significance being asymmetric across the hemispheres, which gets lost when mapping to a common template, or it could also be due to the extra smoothing that the combined STE paradigm causes.

We also can plot the residual pose parameters roughly across the two groups by taking the subset of scans that belong to the control group and calculate the mean structure using general orthogonalized Procrustes analysis, and similarly for the diseased group. By plotting these two mean structures together, we can roughly see pose changes in rotation and translation, and these are shown in Figure 4.1 and Figure 4.2.

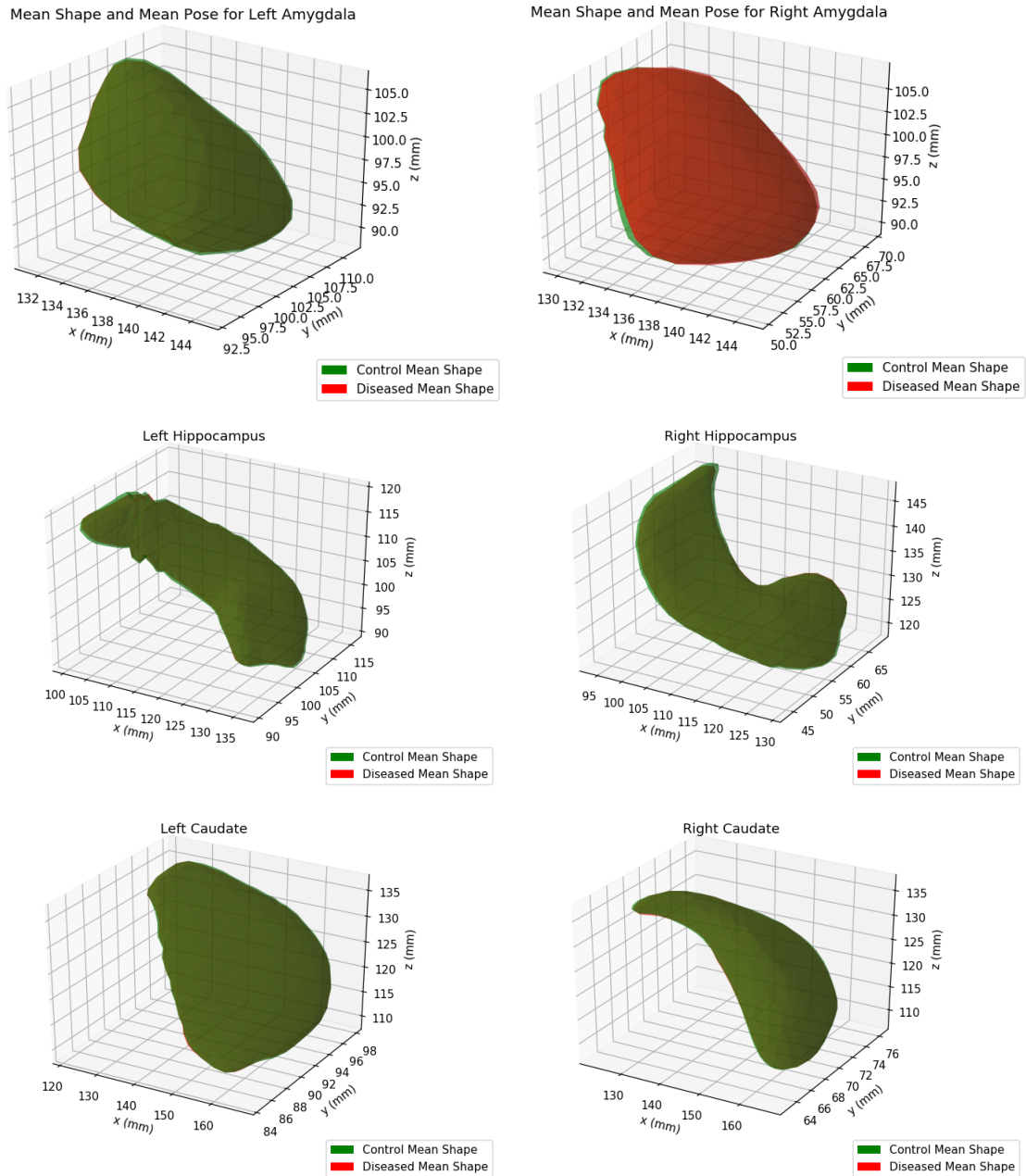


Figure 4.1: Superimposed plots of the calculated Procrustes mean shape for the control group (green) and the diseased group (red); for the Amygdala, Hippocampus, and Caudate

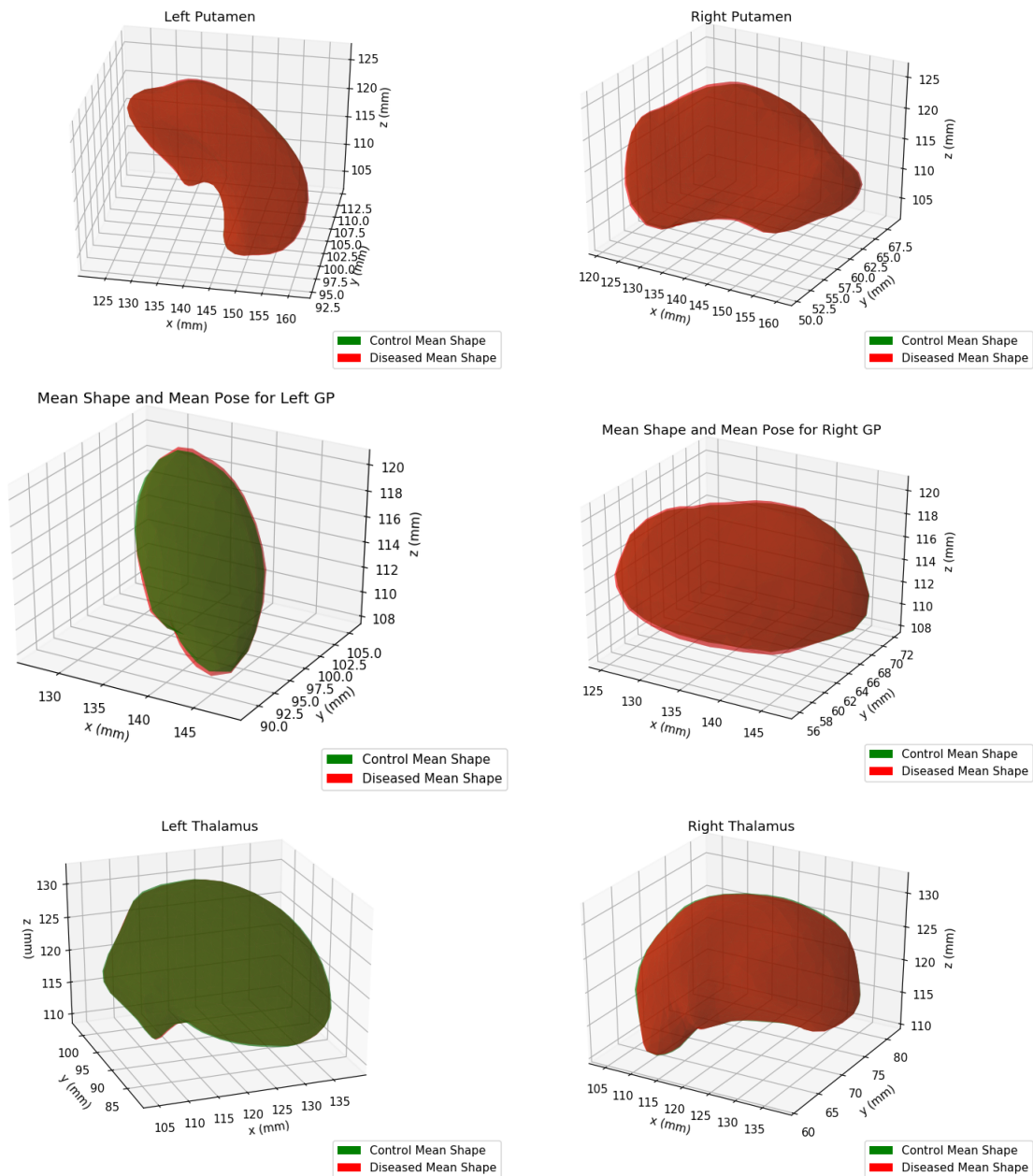


Figure 4.2: Superimposed plots of the calculated Procrustes mean shape for the control group (green) and the diseased group (red); for the Putamen, Globus Pallidum, and Thalamus

From Figure 4.1 and Figure 4.2, there are subcortical structures where the entirety of the structure is not visible, and there is sometimes significant overlap between the control and diseased mean shapes. In order to represent pose differences in a different way, we also plot control and diseased mean shapes together, and take their coronal and axial sections,

in order to show subtler pose changes that are visible in the coronal and axial sections. These are plotted in Figure 4.3 and Figure 4.4.

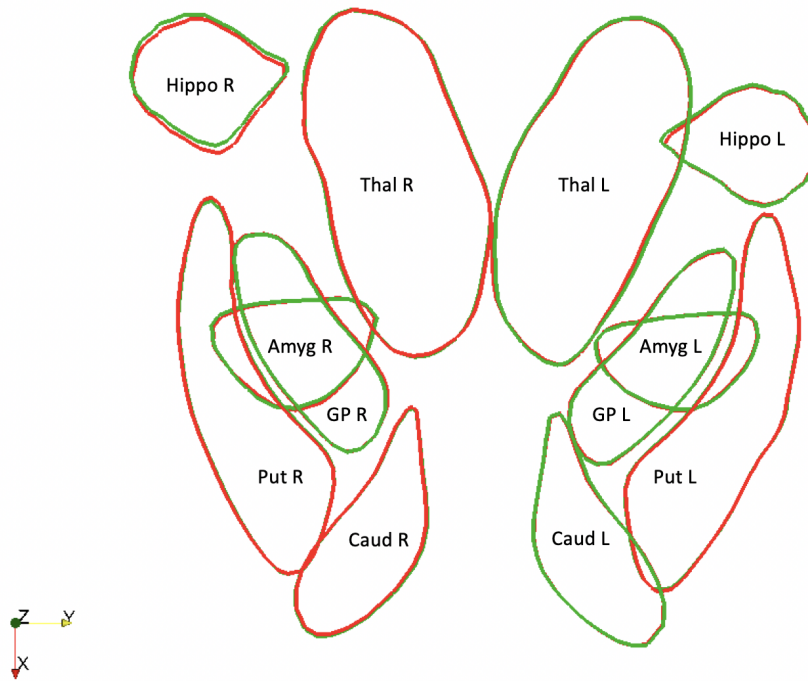


Figure 4.3: Superimposed plots of the calculated Procrustes mean shape for the control group (green) and the diseased group (red) along the axial section

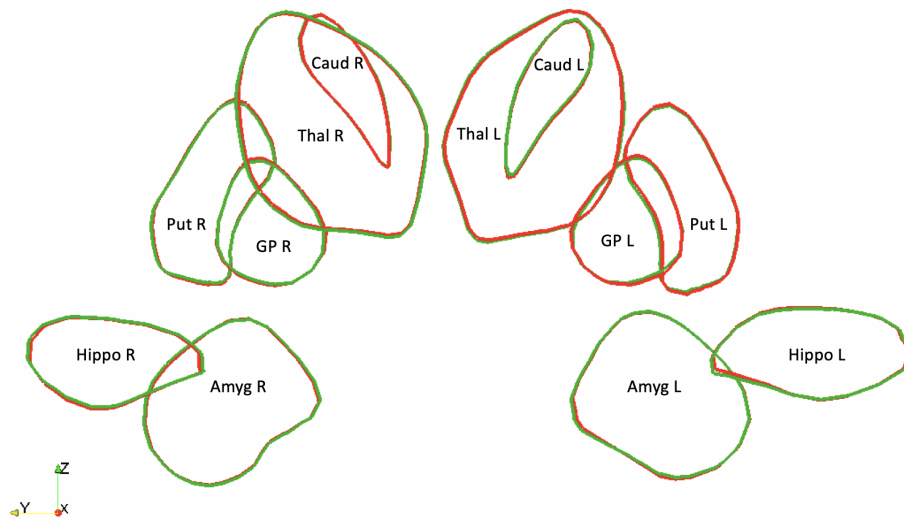


Figure 4.4: Superimposed plots of the calculated Procrustes mean shape for the control group (green) and the diseased group (red) along the coronal section

Chapter 5

Discussion and Conclusion

In this study, we performed a comprehensive and complementary analysis of structural MR scans of patients from the openly available Schizconnect dataset. We looked at meaningful volume, shape, and pose features that can be extracted from these structural MR scans, and studied possible sources of statistical difference across healthy subjects and those with strict schizophrenia. At the same time, by focusing on both shape information and pose information, we attempted to find parallels between these two paradigms of subcortical structure analysis, as well as complementary information that may not be captured individually by either one of the methods of statistical analysis.

From the volume regression plots in chapter 3, we see that the binary segmentation volumes are not monotonically decreasing for any of the 6 subcortical structures under question. Though there is a rough overall downward trend for subjects with exactly two scans, for subjects with three scans, there are cases where subcortical structures do not follow a perfectly monotonic trend, either for the controls or the diseased populations. Though there may be clinically significant reasons for the diseased group not following a perfectly monotonic trend, there is not much support in literature for healthy subject subcortical structure volumes not decreasing monotonically due to ageing effects. This leads us to believe that the initial preprocessing and binary segmentation step may not be

optimal, and may have noise artefacts in the segmentation of the subcortical structures under question. We perform rigorous manual quality control on the subcortical structures that were segmented from the Schizconnect dataset, and even after manually excluding 17 scans where the MRICloud preprocessing pipeline failed in the subcortical segmentation step, we still see the above results in the volume regression analysis.

In order to smooth out noise and artefacts arising from the binary segmentation step, we impose additional regularization during the Delauney triangulation step, in order to constrain the number of vertices that a triangulated surface can consist of, and in general result in a much smoother polygon, in an attempt to address rough or blocky segmentations from the structural MRIs. Upon plotting the volume regressions for the triangulated surfaces, we definitely see an improvement in the monotonicity of the downward volume trends, for both the control and diseased subjects, for most of the subcortical structures. The hippocampus is seen to have an overall upward trend in volume over time, and this is further reflected in the global atrophy analysis done in chapter 3, where the left and right hippocampi are shown to have negative atrophy rates, which correspond to an increase in volume over time. We further extend the volume regression analysis on the triangulated surfaces, by calculating the slopes of the best-fit lines for each volume trend, and then plotting the histograms of these slope distributions over the control and diseased groups. For the histograms we see that there is significant variation in the distribution of slopes, ranging from the negative to the positive. For certain subcortical structures, we can see that the histograms for the diseased group are skewed to either the left or the right, implying that over the population, on average, there are differences in volume atrophy trends between the two groups (right amygdala, right hippocampus, right putamen, left and right globus pallidum, left and right thalamus). However, at the same time, there are certain structures that don't show any differences in the means of the histograms, even if the distributions have different forms, and it is difficult to say if there are any group

differences from the histogram plots themselves. However, seeing the high variance in volume trends alludes to the data having poor preprocessing quality, since at least for the controls, according to clinical findings, all subcortical structures would go down in volume over time due to natural ageing effects. At the same time, we have scans taken 2 years and 4 years apart, and between these scans, there may be enough variance in scan quality and the preprocessing steps that confound the volume trends. Given that for the atrophy rate, we observe an effect size less than one percent of the overall volume of each subcortical structure, across all subcortical structures, the atrophy effects seen in both the controls and diseased subjects may be due to variation in a variety of factors, emerging across the timeline of the scans being taken, such as insufficient control of variates in patients on the day of the scan, the amount of hydration that patients possess on the day of their scan, and intrinsic scanner variability from year to year.

On performing longitudinal analysis on subcortical volumes and surface Jacobians, we find only the thalamus and hippocampus have statistically significant changes across the two groups, and these observations have been reported before in literature (Prestia et al., 2011). At the same time, we also see that in terms of the atrophy rates, both the left and right hippocampi seem to be increasing in size for both the controls and the diseased populations. Though there are some reports of contradictory findings in literature regarding the effect of schizophrenia on the hippocampus, the fact that the control subjects are also going up in volume in time point to possible preprocessing issues with the data. In order to compensate for rough binary segmentations introducing noise to the volume measurements of the data, we also attempted using a combined surface template that pools in the left and right hemisphere scans in order to achieve higher power and more smoothness in the surface template mapping, at the cost of losing information about the hemisphere of the scan. We see that that broadly, the significance in subcortical structures translates over to the combined STE paradigm, and for both the hippocampus and thalamus, there

is an effect of combining regions of significant vertices across the left and right volumes, into a larger, more contiguous region of statistically different surface effects. At the same time, comparing the number of significant vertices for the left and right surface templates versus the combined template, we get a sense of which significant vertices were unique to a specific hemisphere, and which vertices were common across the two, giving us a better idea of the symmetry (or asymmetry) of the effect of schizophrenia on local surface changes.

Finally, in an attempt to obtain complementary information about subcortical volumes under question, we also performed residual pose analysis with the 7 dimensions of the residual pose features. We performed both cross-sectional analysis with the baseline scans, and longitudinal analysis with the entire dataset. From the cross-sectional analysis, we see both similarities and differences to the volumetric and local surface mixed-effects modelling. The amygdala and hippocampi especially show difference in the scale parameters, which correspond well with volumetric differences as well, and the right amygdala has a further translational difference as well. At the same time, we obtain complementary information in the globus pallidum, which had not shown any statistical significance for the volumetric analysis, but has significant global pose differences, which arise due to rotational and translational changes in the structure of the globus pallidum, which may correspond to atrophy around the globus pallidum itself.

At the same time, longitudinal analysis with residual pose parameters results in surprisingly low statistical significance across all subcortical structures, for both the unique STE and combined STE paradigms. There may be a few reasons why this may be the case. Firstly, it is entirely possible that even though pose varies significantly across the cross-sectional population, pose parameters don't change too much over time, as rotational and translational parameters are global-scale changes on the subcortical structures, and these global changes may need more than a 4 year timescale to capture. Compared to local

surface changes and atrophy, a more discrete feature such as pose may not possess enough discriminative ability over a 4 year timescale, and in order to fully utilize residual pose analysis, we may either pick a cross-section of the data, or introduce scans from longer time-periods as well. Secondly, it is possible that changing pose parameters over time may not be very well modelled by a standard mixed-effects models, due to the dependence between translation and rotation parameters. For example, a certain rotation of a subcortical structure over time may increase rotation angles in 2 of the 3 dimensions and reduce it in the third, while also having interactions with translation in the 3 dimensions as well. To summarize, residual pose analysis may be better suited for cross-sectional analysis of populations for the study of a neuronal disease such as schizophrenia, and further research may need to be done on models that better fit the residual pose parameters by understanding the interplay in the spatial parameters.

5.1 Limitations

There are some limitations to this study as well, which have been briefly mentioned above in the Results and Discussions section, which we summarize here. From the preliminary analysis with the volume regression plots, we see that there is significant variation in the distribution of volume change across subjects, which may arise due to noise and artefacts in the preprocessing step, as well as noise in the raw structural MRI scans due to scanner artefacts, patient movement, and patient status during follow-up status etc.

Since we perform morphometric analysis on a schizophrenia dataset, there are several factors that can contribute to the lack of significantly different changes across the two groups; the subjects' medication information is not taken into account when modelling the longitudinal progression of disease, and brain volume can be affected by the type and

quantity of medication being taken by the patients, which is not corrected for. Secondly, the subjects' handedness information and total intracranial volume information are not taken as covariates while modelling size parameters and residual pose parameters, and correcting for these dependent variables could potentially improve statistical modelling of the dataset. Thirdly, since schizophrenia is an early neurodevelopmental disorder, the study would be improved by having patients in the early and late adolescence stage as well, along with subjects with scans over a longer time period, in order to better model the stages of progression of the disease.

Finally, residual pose analysis has a few limitations as well when it comes to modelling longitudinal progression of a disease, since pose parameters are very discrete features and may not show significant differences over a 4 year timescale. Due to the inter-dependence of rotation, translation and scale parameters, it may not be ideal to model them independently, and a more rigorous framework that takes this interplay into account may be more effective. Residual pose analysis also performs better in cross-sectional analysis, where we ignore later scans in the dataset, which does reduce the statistical power of further statistical tests in the cross-sectional analysis, which cannot therefore be compared to a longitudinal analysis of volume and surface Jacobians, which have a higher statistical power and a different modelling of confounding factors.

5.2 Future Work

The focus of this study has been on creating a robust, replicable pipeline for residual pose analysis that can be easily applied to structural MRI data in order to extract meaningful low-dimensional feature representations of high-dimensional 3D voxel data. The first step to extend this analysis would be to apply this pose pipeline to further datasets of schizophrenic and healthy patients, in order to improve the statistical power of both the

cross-sectional and longitudinal analysis. Secondly, combining structural measurements of pose and volume could be paired with brain functionality measurements, especially in probing connecting pathways between the subcortical structures. Further improvements can also be made on the amount of manual and automated quality control being done to the dataset after processing through the MRICloud pipeline, in order to understand why there are fluctuations in volumetric trends in even the control patients processed through the pipeline.

The residual pose pipeline can also be treated as a highly ontological dimensionality reduction technique that converts very high-dimensional medical imaging to highly interpretable 7-dimensional feature vectors. One further direction of research could be to probe the efficacy of this 7-dimensional representation of pose for the task of discrimination between healthy and schizophrenic patients, or adding these features to currently existing volume and shape-based discrimination methods in order to augment these feature representations with complementary data. By enriching volume and shape descriptors with pose, the residual pose technique may have the ability to aid in research that improves our understanding of schizophrenia and other neurodegenerative diseases.

References

- Kessler, Ronald C, Howard Birnbaum, Olga Demler, Ian RH Falloon, Elizabeth Gagnon, Margaret Guyer, Mary J Howes, Kenneth S Kendler, Lizheng Shi, Ellen Walters, et al. (2005). "The prevalence and correlates of nonaffective psychosis in the National Comorbidity Survey Replication (NCS-R)". In: *Biological psychiatry* 58.8, pp. 668–676.
- Vos, Theo, Amanuel Alemu Abajobir, Kalkidan Hassen Abate, Cristiana Abbafati, Kaja M Abbas, Foad Abd-Allah, Rizwan Suliankatchi Abdulkader, Abdishakur M Abdulle, Teshome Abuka Abebo, Semaw Ferede Abera, et al. (2017). "Global, regional, and national incidence, prevalence, and years lived with disability for 328 diseases and injuries for 195 countries, 1990–2016: a systematic analysis for the Global Burden of Disease Study 2016". In: *The Lancet* 390.10100, pp. 1211–1259.
- Shenton, Martha E, Chandlee C Dickey, Melissa Frumin, and Robert W McCarley (2001). "A review of MRI findings in schizophrenia". In: *Schizophrenia research* 49.1-2, pp. 1–52.
- Patel, Krishna R, Jessica Cherian, Kunj Gohil, and Dylan Atkinson (2014). "Schizophrenia: overview and treatment options". In: *Pharmacy and Therapeutics* 39.9, p. 638.
- Siever, Larry J and Kenneth L Davis (2004). "The pathophysiology of schizophrenia disorders: perspectives from the spectrum". In: *American Journal of Psychiatry* 161.3, pp. 398–413.
- Womer, Fay Y, Lei Wang, Kathryn I Alpert, Matthew J Smith, John G Csernansky, Deanna M Barch, and Daniel Mamah (2014). "Basal ganglia and thalamic morphology in schizophrenia and bipolar disorder". In: *Psychiatry Research: Neuroimaging* 223.2, pp. 75–83.
- Van Rheenen, Tamsyn E, Vanessa Cropley, Andrew Zalesky, Chad Bousman, Ruth Wells, Jason Bruggemann, Suresh Sundram, Danielle Weinberg, Roshel K Lenroot, Avril Pereira, et al. (2017). "Widespread volumetric reductions in schizophrenia and schizoaffective patients displaying compromised cognitive abilities". In: *Schizophrenia bulletin* 44.3, pp. 560–574.

- Prestia, Annapaola, Marina Boccardi, Samantha Galluzzi, Enrica Cavedo, Andrea Adorni, Andrea Soricelli, Matteo Bonetti, Cristina Geroldi, Panteleimon Giannakopoulos, Paul Thompson, et al. (2011). "Hippocampal and amygdalar volume changes in elderly patients with Alzheimer's disease and schizophrenia". In: *Psychiatry Research: Neuroimaging* 192.2, pp. 77–83.
- Ellison-Wright, Ian and Ed Bullmore (2010). "Anatomy of bipolar disorder and schizophrenia: a meta-analysis". In: *Schizophrenia research* 117.1, pp. 1–12.
- Mamah, Daniel, Lei Wang, Deanna Barch, Gabriel A de Erausquin, Mokhtar Gado, and John G Csernansky (2007). "Structural analysis of the basal ganglia in schizophrenia". In: *Schizophrenia research* 89.1-3, pp. 59–71.
- Watson, David R, Feng Bai, Suzanne L Barrett, Aidan Turkington, Teresa M Rushe, Ciaran C Mulholland, and Stephen J Cooper (2012). "Structural changes in the hippocampus and amygdala at first episode of psychosis". In: *Brain imaging and behavior* 6.1, pp. 49–60.
- Ebdrup, Bjørn H, Birte Glenthøj, Hans Rasmussen, Bodil Aggernaes, Annika R Langkilde, Olaf B Paulson, Henrik Lublin, Arnold Skimminge, and William Baaré (2010). "Hippocampal and caudate volume reductions in antipsychotic-naive first-episode schizophrenia". In: *Journal of psychiatry & neuroscience: JPN* 35.2, p. 95.
- Heilbronner, Urs, Myrto Samara, Stefan Leucht, Peter Falkai, and Thomas G Schulze (2016). "The longitudinal course of schizophrenia across the lifespan: clinical, cognitive, and neurobiological aspects". In: *Harvard review of psychiatry* 24.2, p. 118.
- Szöke, Andrei, Anca Trandafir, Marie-Estelle Dupont, Alexandre Meary, Franck Schürhoff, and Marion Leboyer (2008). "Longitudinal studies of cognition in schizophrenia: meta-analysis". In: *The British Journal of Psychiatry* 192.4, pp. 248–257.
- Bossa, Matias, Ernesto Zacur, Salvador Olmos, et al. (2011). "Statistical analysis of relative pose information of subcortical nuclei: application on ADNI data". In: *Neuroimage* 55.3, pp. 999–1008.
- Csernansky, John G, Lei Wang, Sarang C Joshi, J Tilak Ratnanather, and Michael I Miller (2004). "Computational anatomy and neuropsychiatric disease: probabilistic assessment of variation and statistical inference of group difference, hemispheric asymmetry, and time-dependent change". In: *Neuroimage* 23, S56–S68.
- Querbes, Olivier, Florent Aubry, Jérémie Pariente, Jean-Albert Lotterie, Jean-François Démonet, Véronique Duret, Michèle Puel, Isabelle Berry, Jean-Claude Fort, Pierre

- Celsis, et al. (2009). "Early diagnosis of Alzheimer's disease using cortical thickness: impact of cognitive reserve". In: *Brain* 132.8, pp. 2036–2047.
- Thompson, Paul M, Kiralee M Hayashi, Rebecca A Dutton, MING-CHANG CHIANG, Alex D Leow, Elizabeth R Sowell, Greig De Zubicaray, James T Becker, Oscar L Lopez, Howard J Aizenstein, et al. (2007). "Tracking Alzheimer's disease". In: *Annals of the New York Academy of Sciences* 1097.1, pp. 183–214.
- Styner, Martin, Jeffrey A Lieberman, Dimitrios Pantazis, and Guido Gerig (2004). "Boundary and medial shape analysis of the hippocampus in schizophrenia". In: *Medical image analysis* 8.3, pp. 197–203.
- Rao, Anil, Paul Aljabar, and Daniel Rueckert (2008). "Hierarchical statistical shape analysis and prediction of sub-cortical brain structures". In: *Medical image analysis* 12.1, pp. 55–68.
- Bossa, Matias N and Salvador Olmos (2006). "Statistical model of similarity transformations: Building a multi-object pose". In: *2006 Conference on Computer Vision and Pattern Recognition Workshop (CVPRW'06)*. IEEE, pp. 59–59.
- Bossa, Matías N and Salvador Olmos (2007). "Multi-object statistical pose+ shape models". In: *2007 4th IEEE International Symposium on Biomedical Imaging: From Nano to Macro*. IEEE, pp. 1204–1207.
- Styner, Martin, Kevin Gorczowski, Tom Fletcher, Ja Yeon Jeong, Stephen M Pizer, and Guido Gerig (2006). "Statistics of pose and shape in multi-object complexes using principal geodesic analysis". In: *International Workshop on Medical Imaging and Virtual Reality*. Springer, pp. 1–8.
- Gorczowski, Kevin, Martin Styner, Ja Yeon Jeong, JS Marron, Joseph Piven, Heather Cody Hazlett, Stephen M Pizer, and Guido Gerig (2010). "Multi-object analysis of volume, pose, and shape using statistical discrimination". In: *IEEE transactions on pattern analysis and machine intelligence* 32.4, pp. 652–661.
- Lao, Yi, Jie Shi, Yalin Wang, Rafeal Ceschin, Darryl Hwang, Marvin D Nelson, Ashok Panigrahy, and Natasha Leporé (2013). "Statistical analysis of relative pose of the thalamus in preterm neonates". In: *Workshop on Clinical Image-Based Procedures*. Springer, pp. 1–9.

Mori, Susumu, Dan Wu, Can Ceritoglu, Yue Li, Anthony Kolasny, Marc A Vaillant, Andreia V Faria, Kenichi Oishi, and Michael I Miller (2016). "MRICloud: delivering high-throughput MRI neuroinformatics as cloud-based software as a service". In: *Computing in Science & Engineering* 18.5, pp. 21–35.

Schizconnect Website. <http://schizconnect.org>.

Wang, Lei, Kathryn Alpert, Vince Calhoun, David Keator, Margaret King, Alexandr Kogan, Drew Landis, Marcelo Tallis, Steven G Potkin, Jessica A Turner, et al. (2015). "Schizconnect: A one-stop web-based resource for large-scale schizophrenia neuroimaging data integration". In: *Schizophrenia Bulletin*. Vol. 41. OXFORD UNIV PRESS GREAT CLARENDON ST, OXFORD OX2 6DP, ENGLAND, S279–S279.

Wang, Lei, Kathryn I Alpert, Vince D Calhoun, Derin J Cobia, David B Keator, Margaret D King, Alexandr Kogan, Drew Landis, Marcelo Tallis, Matthew D Turner, et al. (2016). "SchizConnect: mediating neuroimaging databases on schizophrenia and related disorders for large-scale integration". In: *NeuroImage* 124, pp. 1155–1167.

Tang, Xiaoying, Kenichi Oishi, Andreia V. Faria, Argye E. Hillis, Marilyn S. Albert, Susumu Mori, and Michael I. Miller (2013). "Bayesian Parameter Estimation and Segmentation in the Multi-Atlas Random Orbit Model". In: *PLoS ONE* 8.6. Ed. by Fabio Rapallo, e65591. ISSN: 1932-6203. DOI: [10.1371/journal.pone.0065591](https://doi.org/10.1371/journal.pone.0065591). URL: <http://dx.plos.org/10.1371/journal.pone.0065591>.

Warfield, S.K., K.H. Zou, and W.M. Wells (2004). "Simultaneous Truth and Performance Level Estimation (STAPLE): An Algorithm for the Validation of Image Segmentation". In: *IEEE Transactions on Medical Imaging* 23.7, pp. 903–921. ISSN: 0278-0062. DOI: [10.1109/TMI.2004.828354](https://doi.org/10.1109/TMI.2004.828354). arXiv: [arXiv:1011.1669v3](https://arxiv.org/abs/1011.1669v3). URL: <https://www.ncbi.nlm.nih.gov/pmc/articles/PMC1283110/pdf/nihms2330.pdf><http://ieeexplore.ieee.org/document/1309714/>.

Asman, Andrew J and Bennett A Landman (2012). "Formulating Spatially Varying Performance in the Statistical Fusion Framework". In: *IEEE Transactions on Medical Imaging* 31.6, pp. 1326–1336. ISSN: 0278-0062. DOI: [10.1109/TMI.2012.2190992](https://doi.org/10.1109/TMI.2012.2190992). URL: <http://www.ncbi.nlm.nih.gov/pubmed/22438513><http://www.pubmedcentral.nih.gov/articlerender.fcgi?artid=PMC3368083><http://ieeexplore.ieee.org/document/6170564/>.

Shewchuk, Jonathan, Tamal K Dey, and Siu-Wing Cheng (2016). *Delaunay mesh generation*. Chapman and Hall/CRC.

- Ma, Jun, Michael I Miller, and Laurent Younes (2010). "A bayesian generative model for surface template estimation". In: *Journal of Biomedical Imaging* 2010, p. 16.
- Tward, Daniel J, Chelsea S Sicat, Timothy Brown, Arnold Bakker, Michela Gallagher, Marilyn Albert, Michael Miller, Alzheimer's Disease Neuroimaging Initiative, et al. (2017a). "Entorhinal and transentorhinal atrophy in mild cognitive impairment using longitudinal diffeomorphometry". In: *Alzheimer's & Dementia: Diagnosis, Assessment & Disease Monitoring* 9, pp. 41–50.
- Tward, Daniel, Michael Miller, Alzheimer's Disease Neuroimaging Initiative, et al. (2017). "Unbiased Diffeomorphic Mapping of Longitudinal Data with Simultaneous Subject Specific Template Estimation". In: *Graphs in Biomedical Image Analysis, Computational Anatomy and Imaging Genetics*. Springer, Cham, pp. 125–136.
- Grenander, Ulf and Michael I Miller (1998). "Computational anatomy: An emerging discipline". In: *Quarterly of applied mathematics* 56.4, pp. 617–694.
- Ross, Amy (2004). "Procrustes analysis". In: *Course report, Department of Computer Science and Engineering, University of South Carolina*.
- Arsigny, Vincent, Olivier Commowick, Xavier Pennec, and Nicholas Ayache (2006). "A log-euclidean framework for statistics on diffeomorphisms". In: *International Conference on Medical Image Computing and Computer-Assisted Intervention*. Springer, pp. 924–931.
- Pennec, Xavier, Pierre Fillard, and Nicholas Ayache (2006). "A Riemannian framework for tensor computing". In: *International Journal of computer vision* 66.1, pp. 41–66.
- Keppel, Geoffrey (1991). *Design and analysis: A researcher's handbook*. Prentice-Hall, Inc.
- Davis, Kelly (2003). "Multiple analysis of variance (MANOVA) or multiple analysis of covariance (MANCOVA)". In: *Unpublished manuscript, Education Leadership and Research Department, Louisiana State University*.
- Bates, Douglas, Martin Mächler, Ben Bolker, and Steve Walker (2014). "Fitting linear mixed-effects models using lme4". In: *arXiv preprint arXiv:1406.5823*.
- Dunn, Olive Jean (1961). "Multiple comparisons among means". In: *Journal of the American statistical association* 56.293, pp. 52–64.
- Nichols, Thomas E and Andrew P Holmes (2002). "Nonparametric permutation tests for functional neuroimaging: a primer with examples". In: *Human brain mapping* 15.1, pp. 1–25.

Tward, Daniel Jacob et al. (2017b). "Singular geodesic coordinates for representing diffeomorphic maps in computational anatomy, with application to the morphometry of early Alzheimer's disease in the medial temporal lobe". PhD thesis. Johns Hopkins University.

Curriculum Vitae

Shreyas Padhy was born on August 29, 1995 in Pune, Maharashtra, India. He graduated from the Indian Institute of Technology Delhi with a Bachelors in Technology in Engineering Physics. In his undergraduate research, he focused on forward and inverse problems in electrodynamics, which introduced him to inverse modelling in the context of medical imaging, specifically for optical tomography.

Shreyas began studying Biomedical Engineering at Johns Hopkins University in Baltimore, Maryland, USA, in 2017, and joined the Center for Imaging Science to work in medical imaging for the human brain with Dr. Michael Miller and Dr. J Tilak Ratnanather. His work focused on deep learning methods for classification of Alzheimer's disease, which was followed by developing algorithms for shape and residual pose analysis for schizophrenia. He also helped teach the Introduction to Computational Medicine and Machine Learning for Signal Processing courses in the Fall of 2018. Shreyas will be completing his Masters in Science and Engineering in Biomedical Engineering in May 2019, and will begin working as an AI Resident at Google Brain in Cambridge, Massachusetts in August 2019.